For example, in patients with a heart rate of 80 beats per minute, a temporal resolution of 250 msec is not improved—even with a segmental reconstruction algorithm—which results in increased artifacts in our phantom study. Thus, the functional assessment of certain heart rates may still be less than ideal. A more rapid rotation time (approximately 0.4 seconds per rotation) has been attained with multi-detector row CT (23,34), which will make it possible to shorten and stabilize the temporal resolution with a segmental approach. As a result, functional assessment with multi-detector row CT will be further improved.

Our results reveal good repeatability among multi-detector row CT measurements, especially with a segmental approach, which indicates that determination of LV border with multi-detector row CT and a segmental approach is accurate and reliable. In fact, we did not encounter substantial difficulties due to motion artifacts when determining the LV border, even in patients with a high heart rate. Although there was no significant difference between the mean value of various functional parameters as determined with multi-detector row CT and MR imaging, the Bland-Altman plot reveals wide limits of agreement. In addition, temporal resolution of a segmental reconstruction algorithm is dependent on heart rate, which is not the case with MR imaging. These findings suggest that LV functional measurements obtained with multi-detector row CT and MR imaging may not be interchangeable.

Recent reports show that the use of a β-blocker is effective in lowering heart rates and reducing motion artifacts (31). According to the literature, however, a β-blocker decreases heart rates by an average of only 8 beats per minute (31). In addition, Vogl et al (22) reported that use of a β-blocker did not produce any effect in some patients. Thus, use of a β-blocker is not always effective in the reduction of motion artifacts. In addition, premedication is troublesome in clinical settings, because careful observation and a prolonged stay are required (23); therefore, β-blockers were not routinely used in our institution. Instead, a segmental reconstruction algorithm has been used to improve temporal resolution when the heart rate is high. A segmental approach may not be useful in the precise assessment of coronary arteries, however, especially when the R-R interval is irregular. At present, there is no definitive solution when the heart rate is high and irregular (23). In addition, the use of a β-blocker changes the LV function (47). Thus, functional parameters, with the exception of LV mass, can be unreliable after such premedication. To obtain functional data as added information, use of a β-blocker is unacceptable.

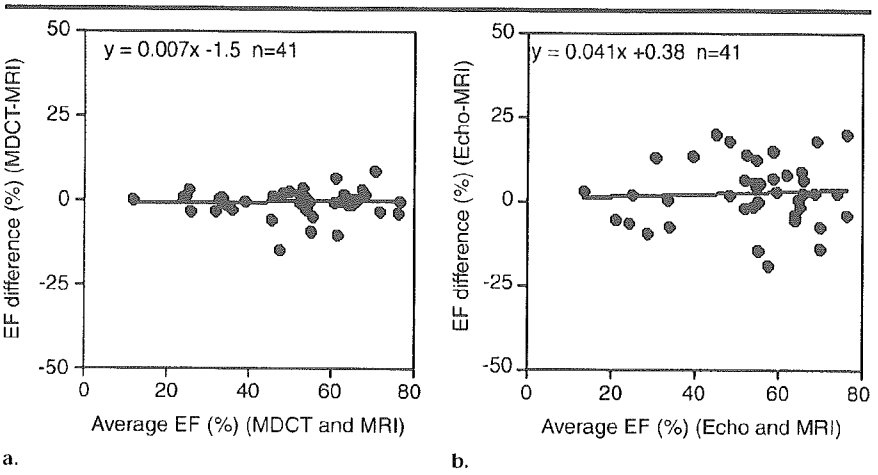

Figure 5. Graphs created with Bland-Altman analysis of LV EF in 41 patients, as measured with (a) multi-detector row CT *(MDCT)* with a segmental reconstruction algorithm and MR imaging or (b) echocardiography and MR imaging. Graphs clearly show that the dispersion between multi-detector row CT and MR imaging was significantly less than that between echocardiography and MR imaging ($P < .001$).

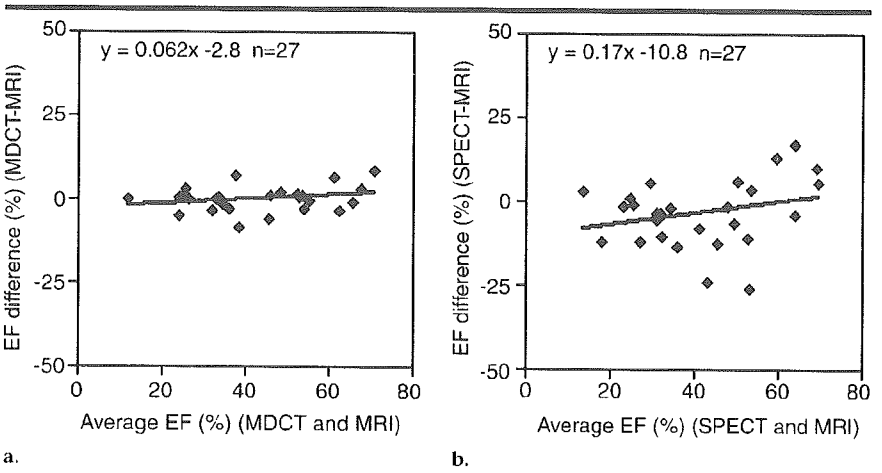

Figure 6. Graphs created with Bland-Altman analysis of LV EF in 27 patients, as measured with (a) multi-detector row CT *(MDCT)* with a segmental reconstruction algorithm and MR imaging or (b) ECG-gated SPECT and MR imaging. Graphs clearly show that the dispersion between multi-detector row CT and MR imaging was significantly less than that between ECG-gated SPECT and MR imaging ($P < .001$).

Radiation dose reduction is clinically important. A large helical pitch, reduced tube current, increased number of detector rows, and faster rotation time can be used to reduce the radiation dose. For example, a larger helical pitch will lead to reduced radiation exposure. When the helical pitch is greater, however, the temporal resolution with a segmental approach becomes worse, which may decrease data fidelity not only for multi-detector row CT coronary information but also for functional analysis. Reduced tube current would serve to directly reduce radiation exposure. Reduced tube current will, however, cause increased image noise. For these reasons, a larger helical pitch or reduced tube current should be avoided (30). Recently, a multi-detector row CT scanner equipped with more detector rows and a faster rotation time has been introduced, resulting in reduction of the radiation dose. In addition, lowering the tube current during unneeded phases of the cycle (48) is effective for radiation dose reduction.

TABLE 9
Linear Regression Analysis between Multi-Detector Row CT and MR Imaging in 50 Patients

Algorithm and Statistics	LV EF	EDV	ESV	LV Mass
Half reconstruction algorithm				
Correlation coefficient	0.93	0.96	0.98	0.95
Standard error of estimates	5.4	17.0	11.4	19.7
Regression line	y = 0.83x + 3.8	y = 0.89x + 17.1	y = 0.91x + 13.0	y = 1.09x − 8.7
Segmental reconstruction algorithm				
Correlation coefficient	0.96	0.97	0.99	0.96
Standard error of estimates	4.4	14.0	8.4	15.4
Regression line	y = 0.97x + 0.5	y = 0.90x + 15.6	y = 0.96x + 4.9	y = 1.01x − 1.1

Note.—Values obtained with multi-detector row CT were closely correlated with those obtained with MR imaging.

TABLE 10
Linear Regression Analysis for EF between Echocardiography and MR Imaging and between Multi-Detector Row CT with a Segmental Reconstruction Algorithm and MR Imaging in 41 Patients

Statistics	Multi-Detector Row CT and MR Imaging	Echocardiography and MR Imaging
Correlation coefficient	0.95	0.84
Standard error of estimates	5.0	9.2
Regression line	y = 0.92x + 2.4	y = 0.84x + 10.5

Note.—Standard error of estimates between multi-detector row CT and MR imaging was significantly less than that between echocardiography and MR imaging ($P < .001$).

TABLE 11
Linear Regression Analysis for EF between ECG-Gated SPECT and MR Imaging and between Multi-Detector Row CT with a Segmental Reconstruction Algorithm and MR Imaging in 27 Patients

Statistics	Multi-Detector Row CT and MR Imaging	ECG-gated SPECT and MR Imaging
Correlation coefficient	0.97	0.83
Standard error of estimates	3.6	8.8
Regression line	y = 1.04x − 1.7	y = 0.97x − 2.2

Note.—Standard error of estimates between multi-detector row CT and MR imaging was significantly smaller than that between ECG-gated SPECT and MR imaging ($P < .001$).

Unfortunately, this strategy may influence the reliability of functional analysis.

The use of multi-detector row CT solely in the assessment of cardiac function does not appear reasonable because of the radiation exposure. It is important, however, that a functional analysis can be conducted by using data obtained with noninvasive coronary imaging without an increase in cost, volume of contrast agent administered, or radiation dose. We believe that multi-detector row CT will be useful in the comprehensive evaluation of coronary arteries and resting LV function.

A limitation of the F test may be the possible violation of the independence assumption, since the variances are about measures taken on the same subject. The critical F values were used for comparison purposes, and statistical significance was not necessarily implied.

In conclusion, the various LV functional parameters of multi-detector row CT with a segmental reconstruction algorithm obtained by using data from several heartbeats correlated and agreed with those obtained with MR imaging. Moreover, the functional analysis with multi-detector row CT with a segmental reconstruction algorithm was more accurate than that with two-dimensional echocardiography or ECG-gated SPECT.

References

1. Buck T, Hunold P, Wentz KU, Tkalec W, Nesser HJ, Erbel R. Tomographic three-dimensional echocardiographic determination of chamber size and systolic function in patients with left ventricular aneurysm. Circulation 1997; 96:4286–4297.
2. Qin JX, Jones M, Shiota T, et al. Validation of real-time three-dimensional echocardiography for quantifying left ventricular volumes in the presence of a left ventricular aneurysm: in vitro and in vivo studies. J Am Coll Cardiol 2000; 36:900–907.
3. Bavelaar-Croon CD, Kayser HW, van der Wall EE, et al. Left ventricular function: correlation of quantitative gated SPECT and MR imaging over a wide range of values. Radiology 2000; 217:572–575.
4. Mochizuki T, Murase K, Higashino H, et al. Two- and three-dimensional CT ventriculography: a new application of helical CT. AJR Am J Roentgenol 2000; 174: 203–208.
5. Lessick J, Sideman S, Azhari H, Marcus M, Grenadier E, Beyar R. Regional three-dimensional geometry and function of left ventricles with fibrous aneurysms: a cine-computed tomography study. Circulation 1991; 84:1072–1086.
6. Lipton MJ, Higgins CB, Farmer D, Boyd DP. Cardiac imaging with a high-speed cine-CT scanner: preliminary results. Radiology 1984; 152:579–582.
7. Lipton MJ, Farmer DW, Killebrew EJ, et al. Regional myocardial dysfunction: evaluation of patients with prior myocardial infarction with fast CT. Radiology 1985; 157:735–740.
8. Rees MR, Feiring AJ, Rumberger JA, MacMillan RM, Clark DL. Heart evaluation by cine CT: use of two new oblique views. Radiology 1986; 159:804–806.
9. Higgins CB. Which standard has the gold? (editorial). J Am Coll Cardiol 1992; 19:1608–1609.
10. Pattynama PM, Lamb HJ, van der Velde EA, van der Wall EE, de Roos A. Left ventricular measurements with cine and spin-echo MR imaging: a study of reproducibility with variance component analysis. Radiology 1993; 187:261–268.
11. Bellenger NG, Burgess MI, Ray SG, et al. Comparison of left ventricular ejection fraction and volumes in heart failure by echocardiography, radionuclide ventricography, cardiovascular magnetic resonance; are they interchangeable? Eur Heart J 2000; 21:1387–1396.
12. de Roos A, Kunz P, Lamb H, et al. Magnetic resonance imaging of ischemic heart disease: why cardiac magnetic resonance imaging will play a significant role in the management of patients with cor-

onary artery disease. J Comput Assist Tomogr 1999; 23(suppl 1):S135–S141.
13. Barkhausen J, Ruehm SG, Goyen M, et al. MR evaluation of ventricular function: true fast imaging with steady-state precession versus fast low-angle shot cine MR imaging: feasibility study. Radiology 2001; 219:264–269.
14. Carr JC, Simonetti O, Bundy J, Li D, Pereles S, Finn JP. Cine MR angiography of the heart with segmented true fast imaging with steady-state precession. Radiology 2001; 219:828–834.
15. Miller S, Simonetti OP, Carr J, Kramer U, Finn JP. MR imaging of the heart with cine true fast imaging with steady-state precession: influence of spatial and temporal resolutions on left ventricular functional parameters. Radiology 2002; 223: 263–269.
16. Heusch A, Koch JA, Krogmann ON, Korbmacher B, Bourgeois M. Volumetric analysis of the right and left ventricle in a porcine heart model: comparison of three-dimensional echocardiography, magnetic resonance imaging and angiography. Eur J Ultrasound 1999; 9:245–255.
17. Lorenz CH, Walker ES, Morgan VL, Klein SS, Graham TP Jr. Normal human right and left ventricular mass, systolic function, and gender differences by cine magnetic resonance imaging. J Cardiovasc Magn Reson 1999; 1:7–21.
18. Tadamura E, Kudoh T, Motooka M, et al. Assessment of regional and global left ventricular function by reinjection Tl-201 SPECT and rest Tc-99m sestamibi ECG-gated SPECT. J Am Coll Cardiol 1999; 33: 991–997.
19. Tadamura E, Kudoh T, Motooka M, et al. Use of technetium-99m sestamibi ECG-gated single-photon emission tomography for the evaluation of left ventricular function following coronary artery bypass graft: comparison with three-dimensional magnetic resonance imaging. Eur J Nucl Med 1999; 26:705–712.
20. Nieman K, Oudkerk M, Rensing BJ, et al. Coronary angiography with multi-slice computed tomography. Lancet 2001; 357:599–603.
21. Achenbach S, Giesler T, Ropers D, et al. Detection of coronary artery stenoses by contrast-enhanced, retrospectively electrocardiographically-gated, multislice spiral computed tomography. Circulation 2001; 103:2535–2538.
22. Vogl TJ, Abolmaali ND, Diebold T, et al. Techniques for the detection of coronary atherosclerosis: multi-detector row CT coronary angiography. Radiology 2002; 223:212–220.
23. Nieman K, Cademartiri F, Lemos PA, Raaijmarkers R, Pattynama PM, Feyter PJ. Reliable noninvasive coronary angiography with fast submillimeter multislice spiral computed tomography. Circulation 2002; 106:2051–2054.
24. Schroeder S, Kopp AF, Baumbach A, et al. Noninvasive detection and evaluation of atherosclelotic coronary plaques with multislice computed tomography. J Am Coll Cardiol 2001; 37:1430–1435.
25. Horiguchi J, Nakanishi T, Ito K. Quantification of coronary artery calcium using multidetector CT and a retrospective ECG-gating reconstruction algorism. AJR Am J Roentgenol 2001; 177:1429–1435.
26. White RD, Setser RM. Integrated approach to evaluating coronary artery disease and ischemic heart disease. Am J Cardiol 2002; 90:49L–55L.
27. Hong C, Becker CR, Schoepf UJ, Ohnesorge B, Bruening R, Reiser MF. Coronary artery calcium: absolute quantification in nonenhanced and contrast-enhanced multi-detector row CT studies. Radiology 2002; 223:474–480.
28. Willmann JK, Weishaupt D, Lachat M, et al. Electrocardiographically gated multi-detector row CT for assessment of valvular morphology calcification in aortic stenosis. Radiology 2002; 225:120–128.
29. Hong C, Becker CR, Huber A, et al. ECG-gated reconstructed multi-detector row CT coronary angiography: effect of varying trigger delay on imaging quality. Radiology 2001; 220:712–717.
30. Kopp AF, Schroeder S, Kuettner A, et al. Coronary arteries: retrospectively ECG-gated multi-detector row CT angiography with selective optimization of the image reconstruction window. Radiology 2001; 221:683–688.
31. Ropers D, Baum U, Pohle K, et al. Detection of coronary artery stenoses with thin-slice multi-detector row spiral computed tomography and multiplanar reconstruction. Circulation 2003; 107:664–666.
32. Juergens KU, Grude M, Fallenberg EM, et al. Using ECG-gated multidetector CT to evaluate global left ventricular myocardial function in patients with coronary artery disease. AJR Am J Roentgenol 2002; 179:1545–1550.
33. Juergens KU, Grude M, Maintz D, et al. Multi–detector row CT of left ventricular function with dedicated analysis software versus MR imaging: initial experience. Radiology 2004; 230:403–410.
34. Halliburton SS, Boese JM, Flohr TG, Lieber ML, Kuzmiak SA, White RD. Improved volumetric analysis of the left ventricle using cardiac multislice computed tomography (MSCT) with high temporal resolution image reconstruction (abstr). Radiology 2002; 225(P):389.
35. Ota T, Taguchi K. A navigation tool to assist optimal scan protocol of electrocardiogram (ECG)-gated retrospective reconstruction for multislice helical CT (abstr). Radiology 2001; 221(P):690.
36. Flohr T, Ohnesorge B. Heart rate adaptive optimization of spatial and temporal resolution for electrocardiogram-gated multislice spiral CT of the heart. J Comput Assist Tomogr 2001; 25:907–923.
37. Takase K, Sawamura Y, Igarashi K, et al. Demonstration of the artery of Adamkiewicz at multidetector row helical CT. Radiology 2002; 223:39–45.
38. Dirksen MS, Bax JJ, de Roos A, et al. Usefulness of dynamic multislice computed tomography of left ventricular function in unstable angina pectoris and comparison with echocardiography. Am J Cardiol 2002; 90:1157–1160.
39. Schiller NB, Acquatella H, Ports TA, et al. Left ventricular volume from paired biplane two-dimensional echocardiography. Circulation 1979; 60:547–555.
40. Gordon EP, Schnittger I, Fitzgerald PJ, Williams P, Popp RL. Reproducibility of left ventricular volumes by two-dimensional echocardiography. J Am Coll Cardiol 1983; 2:506–513.
41. Otterstad JE, Froeland G, St John SM, Holme I. Accuracy and reproducibility of biplane two-dimensional echocardiographic measurements of left ventricular dimensions and function. Eur Heart J 1997; 18:507–513.
42. Takahashi N, Tamaki N, Tadamura E, et al. Combined assessment of regional perfusion and wall motion in patients with coronary artery disease with technetium-99m tetrofosmin. J Nucl Cardiol 1994; 1:29–38.
43. Germano G, Kiat H, Kavanagh PB, et al. Automatic quantification of ejection fraction from gated myocardial perfusion SPECT. J Nucl Med 1995; 36:2138–2147.
44. Bland JM, Altman DG. Statistical methods for assessing agreement between two methods of clinical measurement. Lancet 1986; 1:307–310.
45. Manrique A, Faraggi M, Vera P, et al. Tl-201 and Tc-99m MIBI gated SPECT in patients with large perfusion defects and left ventricular dysfunction: comparison with equilibrium radionuclide angiography. J Nucl Med 1999; 40:805–809.
46. Mazzanti M, Geremano G, Kait H, et al. Identification of severe and extensive coronary artery disease by automatic measurement of transient ischemic dilation of the left ventricle in dual-isotope myocardial perfusion SPECT. J Am Coll Cardiol 1996; 27:1612–1620.
47. Ooi H, Colucci WS. Pharmacological treatment of heart failure. In: Hardmann JG, Limbird LE, Gilman AG, eds. The pharmacological basis of therapeutics. 10th ed. New York, NY: McGraw-Hill, 2001; 913–916.
48. Jakobs TF, Becker CR, Ohnesorge B, et al. Multislice helical CT of the heart with retrospective ECG gating: reduction of radiation exposure by ECG-controlled tube current modulation. Eur Radiol 2002; 12: 1081–1086.

Journal of the American College of Cardiology
© 2005 by the American College of Cardiology Foundation
Published by Elsevier Inc.

Vol. 46, No. 11, 2005
ISSN 0735-1097/05/$30.00
doi:10.1016/j.jacc.2005.08.043

High Risk for Bradyarrhythmic Complications in Patients With Brugada Syndrome Caused by *SCN5A* Gene Mutations

Takeru Makiyama, MD,* Masaharu Akao, MD, PHD,* Keiko Tsuji, BS,* Takahiro Doi, MD,* Seiko Ohno, MD,* Kotoe Takenaka, MD, PHD,* Atsushi Kobori, MD, PHD,* Tomonori Ninomiya, MD, PHD,* Hidetada Yoshida, MD, PHD,* Makoto Takano, MD, PHD,† Naomasa Makita, MD, PHD,‡ Fumiko Yanagisawa, MD,§ Yukei Higashi, MD, PHD,§ Youichi Takeyama, MD, PHD,§ Toru Kita, MD, PHD,* Minoru Horie, MD, PHD‖

Kyoto, Tochigi, Sapporo, Yokohama, and Otsu, Japan

OBJECTIVES We carried out a complete screening of the *SCN5A* gene in 38 Japanese patients with Brugada syndrome to investigate the genotype-phenotype relationship.

BACKGROUND The gene *SCN5A* encodes the pore-forming α-subunit of voltage-gated cardiac sodium (Na) channel, which plays an important role in heart excitation/contraction. Mutations of *SCN5A* have been identified in 15% of patients with Brugada syndrome.

METHODS In 38 unrelated patients with clinically diagnosed Brugada syndrome, we screened for *SCN5A* gene mutations using denaturing high-performance liquid chromatography and direct sequencing, and conducted a functional assay for identified mutations using whole-cell patch-clamp in heterologous expression system.

RESULTS Four heterozygous mutations were identified (T1871, D356N, K1578fs/52, and R1623X) in 4 of the 38 patients. All of them had bradyarrhythmic complications: three with sick sinus syndrome (SSS) and the other (D356N) with paroxysmal complete atrioventricular block. *SCN5A*-linked Brugada patients were associated with a higher incidence of bradyarrhythmia (4 of 4) than non–*SCN5A*-linked Brugada patients (2 of 34). Families with T1871 and K1578fs/52 had widespread penetrance of SSS. Notably, the patient with K1578fs/52, who had been diagnosed as having familial SSS without any clinical signs of Brugada syndrome, showed a Brugada-type ST-segment elevation after intravenous administration of pilsicainide and programmed electrical stimulation-induced ventricular tachycardia. All of the mutations encoded non-functional Na channels, and thus were suggested to cause impulse propagation defect underlying bradyarrhythmias.

CONCLUSIONS Our findings suggest that loss-of-function *SCN5A* mutations resulting in Brugada syndrome are distinguished by profound bradyarrhythmias. (J Am Coll Cardiol 2005;46:2100–6)
© 2005 by the American College of Cardiology Foundation

Brugada syndrome is an inherited disorder, characterized by sudden death from ventricular tachyarrhythmias especially during sleep, ST-segment elevation in the right precordial leads, and conduction slowing in the absence of structural heart disease (1,2). In approximately 15% of Brugada patients, mutations of the *SCN5A* gene, which encodes the pore-forming α-subunit of voltage-gated cardiac sodium (Na) channel, have been identified, and functional analyses for some of these mutations revealed a loss-of-function type modulation (3–6). Because Na current plays a key role in heart excitation/contraction, functional changes in these channels can cause a variety of cardiac phenotypes. Interestingly, mutations of *SCN5A* have been reported to generate several types of disease entities distinct from Brugada syndrome: congenital type 3 long-QT syndrome (7), idiopathic ventricular fibrillation (VF) (8), progressive cardiac conduction defect (PCCD) (9), congenital sick sinus syndrome (SSS) (10), atrial fibrillation (11), and even overlap syndrome (12,13).

In this study, we carried out a complete screening of the *SCN5A* gene in 38 Japanese Brugada patients to investigate the genotype-phenotype relationship.

METHODS

Study subjects. This study enrolled 38 clinically diagnosed Japanese Brugada syndrome patients (all were unrelated probands). The protocol for genetic analysis was approved by the institutional ethics committee and was performed under its guidelines. All patients provided an informed consent before the genetic analysis. The diagnosis of Brugada syndrome was based on the presence of ST-segment elevation ≥2 mm in leads V_1 through V_3 at baseline or after administration of intravenous Na channel blockers (e.g., pilsicainide) (14). The presence of

From the *Department of Cardiovascular Medicine, Kyoto University Graduate School of Medicine, Kyoto, Japan; †Division of Biophysics, Department of Physiology, Jichii Medical School, Tochigi, Japan; ‡Department of Cardiovascular Medicine, Hokkaido University Graduate School of Medicine, Sapporo, Japan; §Division of Cardiology, Showa University Fujigaoka Hospital, Yokohama, Japan; and the ‖Department of Cardiovascular and Respiratory Medicine, Shiga University of Medical Science, Otsu, Japan. This work is supported by research grants from the Ministry of Education, Science, Sports and Culture of Japan (#16209025) and the Ministry of Health, Labour, and Welfare for Clinical Research for Evidence-Based Medicine (#1508041).

Manuscript received February 23, 2005; revised manuscript received July 29, 2005, accepted August 1, 2005.

Abbreviations and Acronyms

AVB = atrioventricular block
DHPLC = denaturing high-performance liquid chromatography
$h\beta_1$ = human β_1-subunit
PCCD = progressive cardiac conduction defect
SSS = sick sinus syndrome
VF = ventricular fibrillation
VT = ventricular tachycardia

right ventricular cardiomyopathy was excluded by echocardiography. We defined diagnosis of SSS as having a documented sinus pause ≥3 s or chronic sinus bradycardia with a heart rate <50 beats/min.

Deoxyribonucleic acid isolation and mutation analysis. The methods of DNA isolation and mutation analysis were described elsewhere (15). Genetic screening was performed for *SCN5A* by denaturing high-performance liquid chromatography (DHPLC) using a WAVE System Model 3500 (Transgenomic, Omaha, Nebraska).

Site-directed mutagenesis and electrophysiology. With regard to the novel *SCN5A* mutations we identified, site-directed mutagenesis was employed to construct mutants (15). The human cell line HEK293 was transiently transfected with either wild-type human cardiac Na channel α subunit (hH_1) or mutant cDNA by the LipofectAMINE method according to the manufacturer's instructions (Invitrogen, Carlsbad, California) in combination with a bicistronic plasmid (pEGFP-IRES-$h\beta_1$) encoding enhanced green fluorescent protein and the human β_1-subunit ($h\beta_1$) to visually identify cells expressing heterologous $h\beta_1$.

Sodium currents were recorded 24 to 48 h after transfection using the whole-cell patch-clamp technique and analyzed, as we previously described (15). Functional expression studies were performed on multiple independent recombinants.

RESULTS

Mutation analysis. Table 1 shows clinical characteristics of 38 patients with Brugada syndrome enrolled in this study

Table 1. Clinical Characteristics of the Probands (n = 38)

Men/women	35/3
Age (yrs)	47.4 ± 17.0
Family history of SCD	8 (21.1%)
Symptomatic	20 (52.6%)
SSS	5 (13.2%)
pAf	10 (26.3%)
VT or VF	
Documented	9 (23.7%)
Induced	22/27 (81.5%)
ICD implantation	23 (60.5%)

Values are mean ± SD for age. Age represents the age at which diagnosis of Brugada syndrome was made.

ICD = implantable cardioverter-defibrillator; pAf = paroxysmal atrial fibrillation; SCD = sudden cardiac death; SSS = sick sinus syndrome; VF = ventricular fibrillation; VT = ventricular tachycardia.

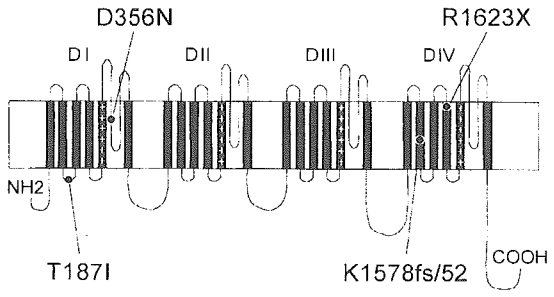

Figure 1. Topology of the voltage-gated sodium (Na) channel. Scheme of the transmembrane topology of the cardiac Na channel illustrating the location of four mutations found in our study. The cardiac Na channel α-subunit consists of four domains (DI through DIV), each containing six transmembrane-spanning segments.

(35 men/3 women, 20 symptomatic/18 asymptomatic, mean age 47.4 ± 17.0 years). A total of 35 probands were already documented with Brugada-type ST-segment elevation at rest (19 symptomatic/16 asymptomatic). The others (three probands) displayed ST-segment elevation after intravenous administration of pilsicainide. Of 18 asymptomatic Brugada patients, 16 underwent programmed electrical stimulation and 15 of them displayed ventricular tachycardia (VT) or VF. Five patients were associated with SSS.

We identified four heterozygous *SCN5A* mutations in four unrelated patients: T187I (c559t), D356N (g1066a), K1578fs/52 (4729 aa insertion), and R1623X (c4864t). Figure 1 shows the positions of identified mutations. K1578fs/52 is a frame-shift mutation resulting in early truncation of the channel protein. R1623X is a nonsense mutation that changes an arginine for a stop codon. The results of DHPLC and DNA sequencing were presented in Figure 2. Three (T187I, D356N, K1578fs/52) were novel and the other (R1623X) was reported to cause congenital SSS in combination with T220I (10). None of these mutations was found in 110 normal control individuals (220 chromosomes). Consistent with a previous report (4), the incidence of *SCN5A* mutations in the Brugada syndrome patients we studied was approximately 10% (4 of 38).

Clinical features. FAMILY K-115 (T187I). The proband, a 33-year-old man, in the family K-115 experienced syncope in his febrile state, and VF was documented. His electrocardiogram (ECG) at rest displayed a typical Brugada syndrome pattern (Fig. 3A, left). After the implantation of a cardioverter-defibrillator, he showed sinus bradyarrhythmia with occasional ventricular pacing (second beat in Fig. 3A, right), indicating the complication of SSS. His affected mother also suffered from SSS and underwent a pacemaker implantation (Fig. 4A).

FAMILY K-54 (D356N). The proband, a 62-year-old man, in the family K-54 had recurrent syncope at age 61. He showed a coved-type ST-segment elevation in the right precordial leads (Fig. 3B), and VF was induced when he underwent an electrophysiological study. During hospitalization, a complete atrioventricular block (AVB) was recorded when he experienced faintness. He had no

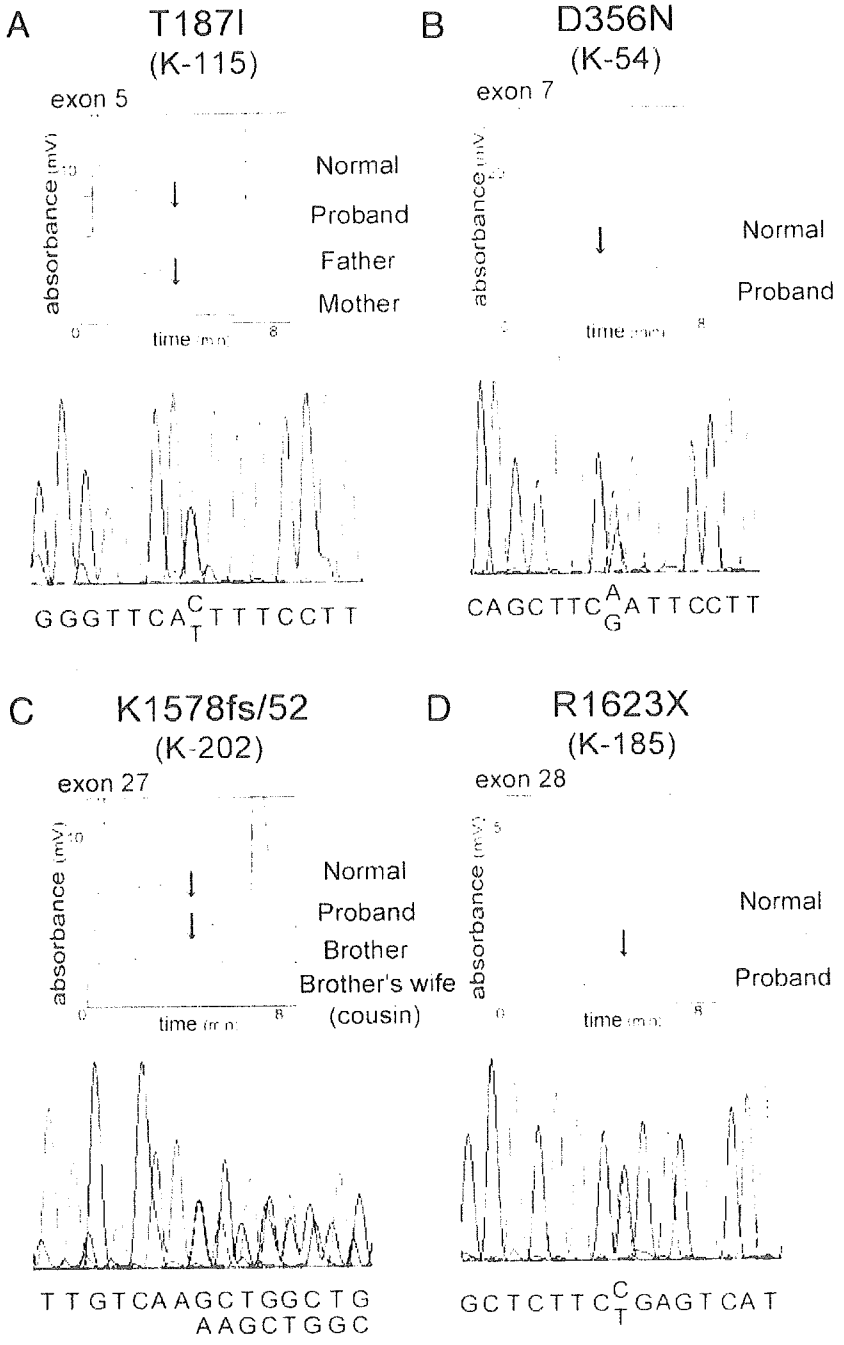

Figure 2. Denaturing high-performance liquid chromatography (DHPLC) analysis and deoxyribonucleic acid (DNA) sequencing. **(Top panels of A through D)** DHPLC confirms abnormal migration patterns in the affected individuals. **(Bottom panels of A through D)** Automated DNA sequencing electropherograms demonstrate mutations in each proband.

family history of lethal arrhythmia or sudden cardiac death (Fig. 4B). His family members refused genetic examinations.

FAMILY K-202 (K1578FS/52). A 68-year-old man (III-6, Fig. 4C) who had received a pacemaker (AAI pacing) due to SSS at age 52 experienced repetitive syncope. His ECG on admission showed a severe sinus arrest because of pacemaker pacing and sensing failure. Three members of his family (III-4, III-7, and IV-1) also suffered from SSS and received a pacemaker, and one affected brother (III-2) had first-degree AVB. One of them, a younger sister (III-7) of the proband, died suddenly even after the pacemaker implantation. In order to assess the association with cardiac Na channelopathies, the proband underwent a pilsicainide challenge test. Intravenous pilsicainide (30 mg) produced a marked prolongation of the PQ interval (240 ms → 320 ms) and revealed a typical Brugada-type ST-segment elevation in the right precordial leads (Fig. 3C, upper panels). Electrophysiological study induced monomorphic VT (Fig. 3C, lower panel). Then he was diagnosed as having Brugada

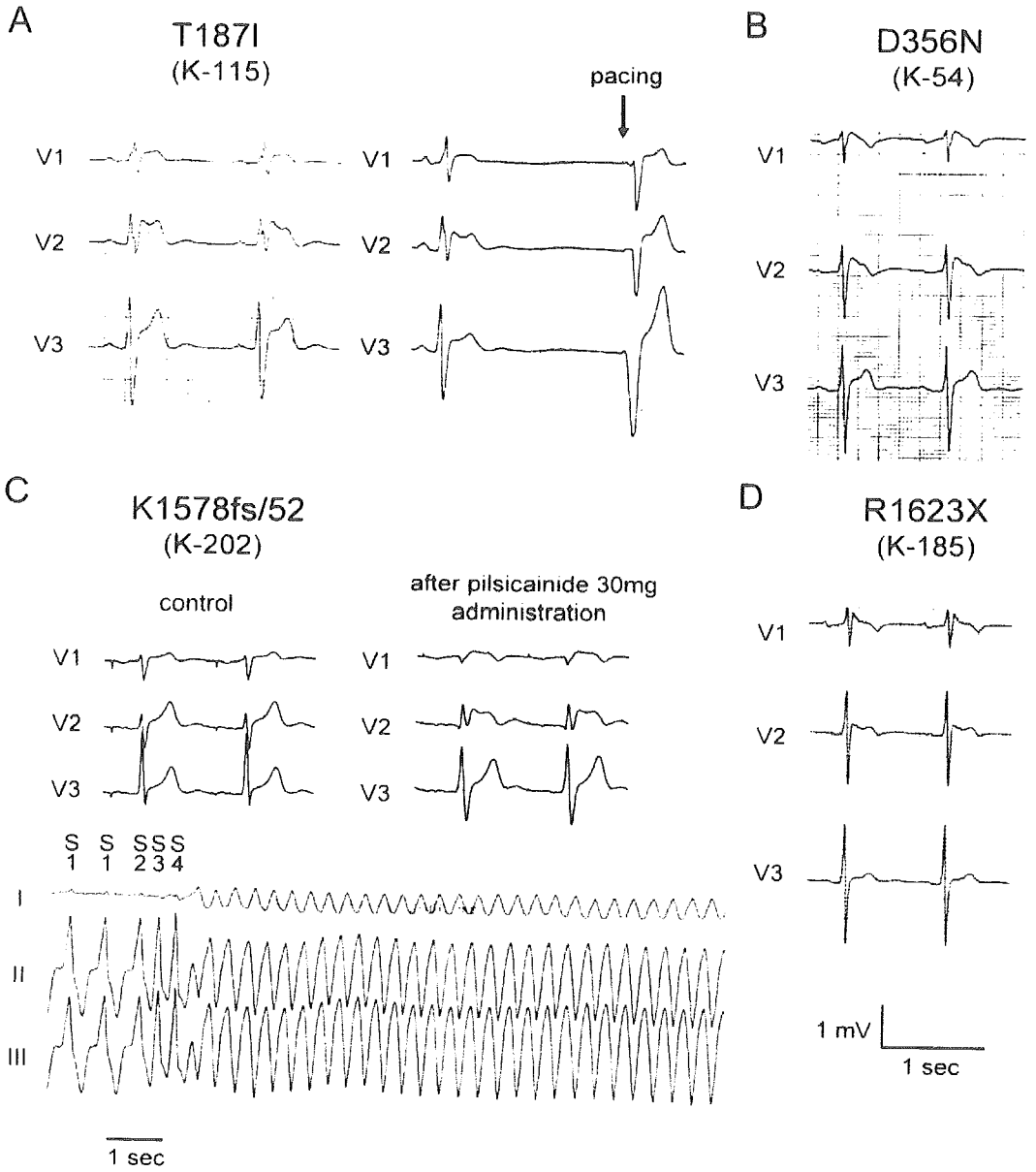

Figure 3. Electrocardiogram (ECG) recordings. **(A through D)** ECG recordings (V_1 through V_3) obtained from the probands. **(Bottom panel of C)** Programmed electrical stimulation (S1-S1/S1-S2/S2-S3/S3-S4 = 600/280/260/240 [ms]) at the right ventricular outflow tract induced monomorphic ventricular tachycardia.

syndrome along with SSS and subsequently received an implantable cardioverter-defibrillator.

FAMILY K-185 (R1623X). The proband was a 65-year-old man who experienced recurrent syncope due to sinus arrest for >5 s at age 61 years and received a pacemaker. At age 65 years, he had faintness due to VF at night and was successfully resuscitated by electric defibrillation. His ECG showed a coved-type ST-segment elevation in the precordial leads (Fig. 3D). His family members refused an ECG and genetic analyses.

Functional analysis of *SCN5A* T187I, D356N, K1578fs/52, and R1623X. We performed biophysical assays for the four novel mutations using a heterologous expression system in HEK293 cells. The protocol is given schematically in Figure 5. Figure 5A illustrates representative whole-cell current traces from cells expressing wild-type (WT), T187I, D356N, K1578fs/52, or R1623X Na channels in the presence of the coexpressed hβ_1. None of the mutants showed an inward Na current, indicating that all of the mutations were non-functional. Reportedly, incubation with mexiletine rescued the reduced current density of a mutant Na channel (M1766L) (16). We, therefore, incubated transfected cells in medium containing 500 μmol/l mexiletine, but failed to rescue the expression of these mutants (data not shown).

The four mutations were all heterozygous. To assess the functional interaction between WT and mutant Na channels, we coexpressed the same amount of both plasmids in

JACC Vol. 46, No. 11, 2005
December 6, 2005:2100–6

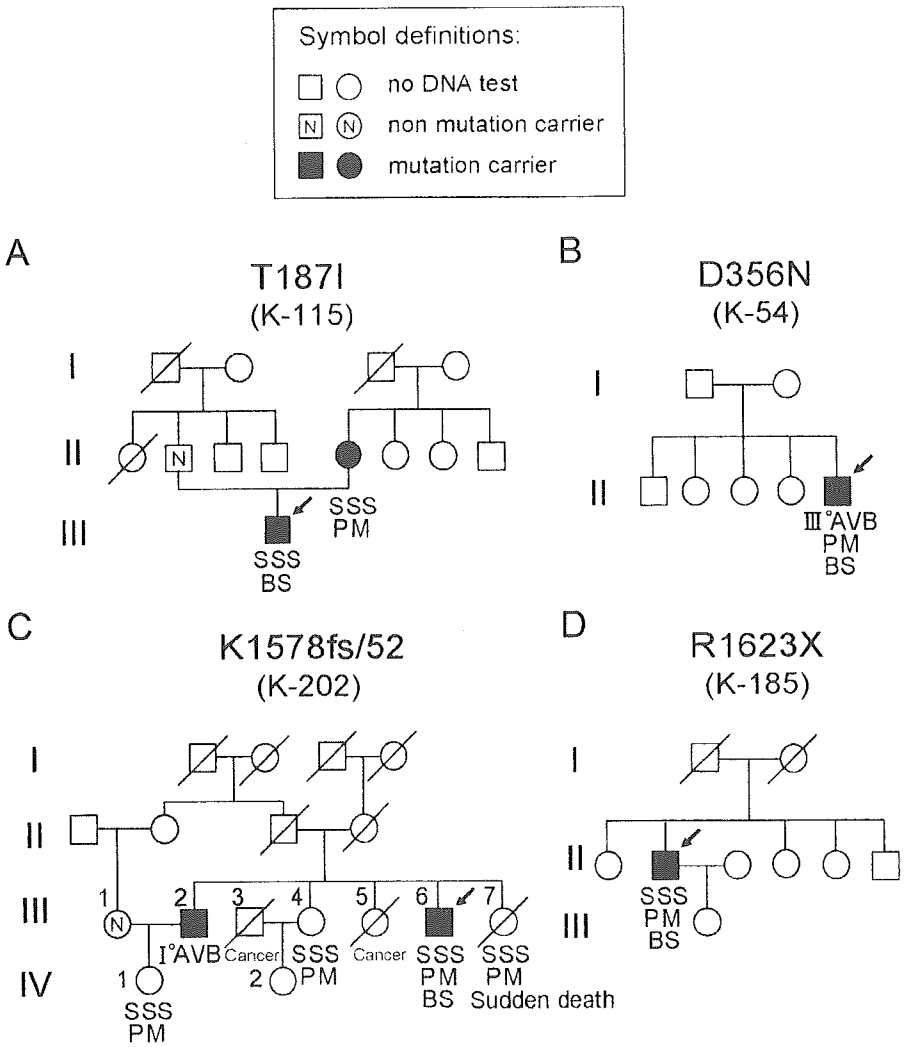

Figure 4. **(A through D)** Pedigrees are shown. **Circles** represent female subjects and **squares** represent male subjects. The **arrowhead** indicates the proband. **Diagonal bars** indicate deceased family members. Members carrying the mutation are represented by **solid circles** or **solid squares**. Further explanation is given in the figure. AVB = atrioventricular block; BS = Brugada syndrome; PM = patients with a pacemaker; SSS = sick sinus syndrome.

combination with hβ_1 in HEK293 cells. Figures 5B and 5C show voltage-dependence of steady-state inactivation/activation and the peak currents. None of the mutants changed channel open probability or current densities, suggesting that the mutants have no dominant-negative effect on WT channels.

DISCUSSION

In this report, we identified four loss-of-function *SCN5A* mutations, T187I, D356N, K1578fs/52, and R1623X in 38 consecutive, unrelated cases of Brugada syndrome in Japan. All four probands were complicated with bradyarrhythmia, such as SSS or AVB. None of these probands had additional *SCN5A* mutations, suggesting that this type of "loss-of-function" overlap syndrome (Brugada syndrome plus SSS/AVB) may result from a single *SCN5A* mutation; SSS was documented in 5 of 38 Brugada patients (Table 1), and *SCN5A* mutations were found in more than half of these five patients (3 of 5), indicating that the patients with the overlap syndrome had a high probability of *SCN5A* mutations.

In patients with Brugada syndrome, several dozen *SCN5A* mutations have been reported to date, and the functional analysis of these mutations revealed a "loss-of-function" type modulation of the α-subunit of Na channels. The severity of channel dysfunction can be variable in terms of channel conductance or gating properties, depending on the types of mutation. Importantly, as shown in Figure 5A, all of the mutations that we identified in the present study were entirely non-functional, and had no dominant-negative effect on WT channels. This complete suppression of Na channel function may be associated with the profound conduction disturbance, and thus bradyarrhythmic phenotypes.

The loss-of-function type mutations of *SCN5A* are reportedly responsible for not only Brugada syndrome but also PCCD (9,17,18), congenital SSS (10), and overlap syndrome (Brugada syndrome plus atrial standstill or sinus node dysfunction) (19,20), supporting the concept that

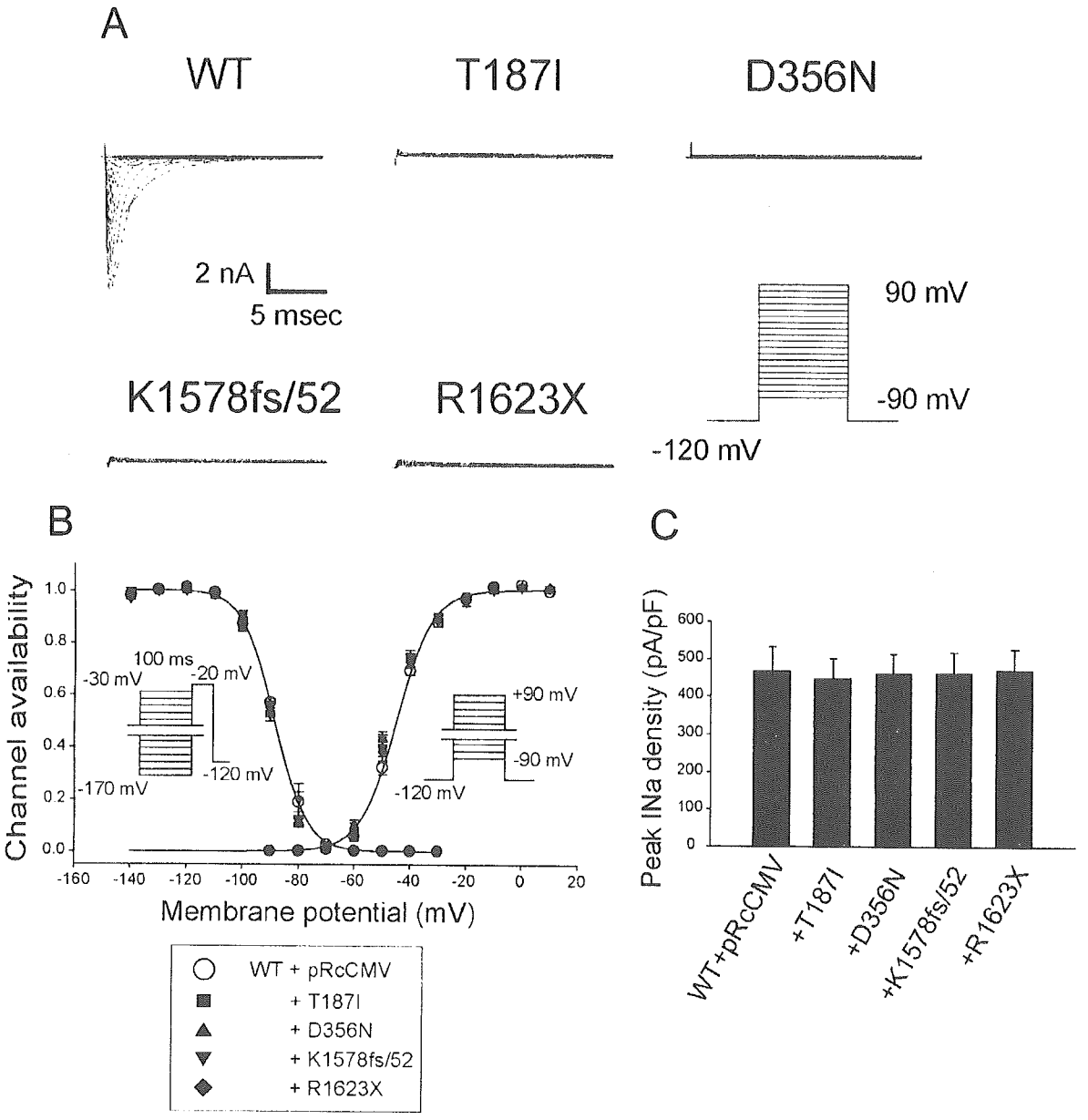

Figure 5. Biophysical assay. **(A)** Whole-cell current recordings of wild-type (WT) and mutant sodium (Na) channels. Sodium channels were expressed with transient transfection in HEK293 cells in the presence of $h\beta_1$. Currents were recorded at various membrane potentials from −90 to +90 mV in 10-mV increments from a holding potential of −120 mV. No currents were detected in cells expressing each mutant. **(B)** Voltage dependence of steady-state inactivation and activation of mutant Na channels cotransfected with WT (mutant-hH_1 [or pRcCMV as a control to adjust the total amount of DNA]: WT-hH_1: $h\beta_1$ = 1:1:1). The curve was fit with the Boltzmann equation: $I/I_{max} = [1+\exp((V-V_{1/2})/k)^{-1}]$. **(C)** Current densities of mutant Na channels. Na currents were elicited at −30 mV from a holding potential of −120 mV. hH_1 = human cardiac Na channel α-subunit.

Brugada syndrome and its bradyarrhythmic complications are caused by a single *SCN5A* mutation. The cellular mechanism for bradyarrhythmias is either a slowing of pacemaker activity or a reduction in impulse propagation. The former seems to be unlikely, because the pacemaker current in sinus nodal cells is largely regulated by calcium and potassium channels, with a minor contribution of Na channels (21,22). Sodium channels in the center of the mouse sinus node consist of tetrodotoxin-sensitive brain-type α-subunits, not tetrodotoxin-insensitive heart-type α-subunits encoded by *Scn5a*, a mouse homologue of *SCN5A* (23). In addition, however, *Scn5a*-coded Na channels were recently reported to play a role in sinus node pacemaking in mice (24). Meanwhile, the latter scenario may be likely; a functional defect of the Na channel can result in a reduction of impulse propagation in the vicinity of the sinus node. Indeed, *Scn5a*-coded Na channels were distributed in the periphery of the mouse sinus node (24), and heterozygous *Scn5a* knockout mice showed a prolongation of the P wave as well as the PR interval, suggesting slow conduction within the atria and atrioventricular conduction system (25). Furthermore, a failure in impulse conduction in

the adjacent atrial myocardium (exit block) is one of the pathophysiological bases of human SSS (26,27).

Benson et al. (10) recently reported a young man with congenital SSS who had compound heterozygous *SCN5A* mutations, T220I and R1623X. Three members of his family had R1623X alone, and showed only subclinical ECG abnormality (first-degree AVB). On the other hand, our R1623X case (K-185), despite the absence of additional mutations, demonstrated more prominent phenotypes; not only SSS but also typical symptomatic Brugada syndrome with spontaneous VF episode. These apparent discrepancies in clinical features may suggest the presence of environmental or other genetic factors modifying the phenotypes.

Notably, we found a frame-shift *SCN5A* mutation (K1578fs/52) in a familial SSS case (K-202). Four family members, including the proband, had received a pacemaker after being diagnosed with SSS. To assess the association with Na channel dysfunction in this SSS case, we carried out a pilsicainide provocation test. A low dose of intravenous pilsicainide induced a Brugada-type elevation in ST and programmed electrical stimulation-provoked VT. This case provides an important insight into the potential overlap between SSS and Brugada syndrome. In familial *SCN5A*-linked SSS cases, the presence of asymptomatic Brugada syndrome may have to be taken into consideration.

In summary, our studies showed Brugada plus bradyarrhythmias (SSS/AVB) type of overlap syndrome was caused by single *SCN5A* mutations that result in a complete loss-of-function in cardiac Na channels. In order to reveal the cellular and molecular mechanisms by which *SCN5A* mutations produce a variety of phenotypes, further studies will be needed, including the establishment of animal models of cardiac Na channelopathies.

Acknowledgment

The authors thank Dr. Alfred L. George, Jr. (Vanderbilt University, Nashville, Tennessee), for providing them with hH_1 cDNA.

Reprint requests and correspondence: Dr. Minoru Horie, Department of Cardiovascular and Respiratory Medicine, Shiga University of Medical Science, Seta Tsukinowa-cho, Otsu, Shiga, 520-2192, Japan. E-mail: horie@belle.shiga-med.ac.jp.

REFERENCES

1. Brugada P, Brugada J. Right bundle branch block, persistent ST-segment elevation and sudden cardiac death: a distinct clinical and electrocardiographic syndrome. A multicenter report. J Am Coll Cardiol 1992;20:1391–6.
2. Brugada J, Brugada P. Further characterization of the syndrome of right bundle branch block, ST-segment elevation, and sudden cardiac death. J Cardiovasc Electrophysiol 1997;8:325–31.
3. Chen Q, Kirsch GE, Zhang D, et al. Genetic basis and molecular mechanism for idiopathic ventricular fibrillation. Nature 1998;392:293–6.
4. Priori SG, Napolitano C, Gasparini M, et al. Clinical and genetic heterogeneity of right bundle branch block and ST-segment elevation syndrome: a prospective evaluation of 52 families. Circulation 2000; 102:2509–15.
5. Antzelevitch C. The Brugada syndrome: ionic basis and arrhythmia mechanisms. J Cardiovasc Electrophysiol 2001;12:268–72.
6. Balser JR. The cardiac sodium channel: gating function and molecular pharmacology. J Mol Cell Cardiol 2001;33:599–613.
7. Bennett PB, Yazawa K, Makita N, George AL Jr. Molecular mechanism for an inherited cardiac arrhythmia. Nature 1995;376:683–5.
8. Akai J, Makita N, Sakurada H, et al. A novel *SCN5A* mutation associated with idiopathic ventricular fibrillation without typical ECG findings of Brugada syndrome. FEBS Lett 2000;479:29–34.
9. Schott JJ, Alshinawi C, Kyndt F, et al. Cardiac conduction defects associate with mutations in *SCN5A*. Nat Genet 1999;23:20–1.
10. Benson DW, Wang DW, Dyment M, et al. Congenital sick sinus syndrome caused by recessive mutations in the cardiac sodium channel gene (*SCN5A*). J Clin Invest 2003;112:1019–28.
11. Olson TM, Michels VV, Ballew JD, et al. Sodium channel mutations and susceptibility to heart failure and atrial fibrillation. JAMA 2005; 293:447–54.
12. Bezzina C, Veldkamp MW, van Den Berg MP, et al. A single Na^+ channel mutation causing both long-QT and Brugada syndromes. Circ Res 1999;85:1206–13.
13. Veldkamp MW, Wilders R, Baartscheer A, Zegers JG, Bezzina CR, Wilde AA. Contribution of sodium channel mutations to bradycardia and sinus node dysfunction in LQT3 families. Circ Res 2003;92: 976–83.
14. Brugada R, Brugada J, Antzelevitch C, et al. Sodium channel blockers identify risk for sudden death in patients with ST-segment elevation and right bundle branch block but structurally normal hearts. Circulation 2000;101:510–5.
15. Shirai N, Makita N, Sasaki K, et al. A mutant cardiac sodium channel with multiple biophysical defects associated with overlapping clinical features of Brugada syndrome and cardiac conduction disease. Cardiovasc Res 2002;53:348–54.
16. Valdivia CR, Ackerman MJ, Tester DJ, et al. A novel *SCN5A* arrhythmia mutation, M1766L, with expression defect rescued by mexiletine. Cardiovasc Res 2002;55:279–89.
17. Tan HL, Bink-Boelkens MT, Bezzina CR, et al. A sodium-channel mutation causes isolated cardiac conduction disease. Nature 2001;409: 1043–7.
18. Wang DW, Viswanathan PC, Balser JR, George AL Jr., Benson DW. Clinical, genetic, and biophysical characterization of *SCN5A* mutations associated with atrioventricular conduction block. Circulation 2002;105:341–6.
19. Takehara N, Makita N, Kawabe J, et al. A cardiac sodium channel mutation identified in Brugada syndrome associated with atrial standstill. J Intern Med 2004;255:137–42.
20. Smits JP, Koopmann TT, Wilders R, et al. A mutation in the human cardiac sodium channel (E161K) contributes to sick sinus syndrome, conduction disease and Brugada syndrome in two families. J Mol Cell Cardiol 2005;38:969–81.
21. Kodama I, Nikmaram MR, Boyett MR, Suzuki R, Honjo H, Owen JM. Regional differences in the role of the Ca^{2+} and Na^+ currents in pacemaker activity in the sinoatrial node. Am J Physiol 1997;272: H2793–806.
22. Boyett MR, Honjo H, Kodama I. The sinoatrial node, a heterogeneous pacemaker structure. Cardiovasc Res 2000;47:658–87.
23. Maier SK, Westenbroek RE, Yamanushi TT, et al. An unexpected requirement for brain-type sodium channels for control of heart rate in the mouse sinoatrial node. Proc Natl Acad Sci U S A 2003;100:3507–12.
24. Lei M, Jones SA, Liu J, et al. Requirement of neuronal- and cardiac-type sodium channels for murine sinoatrial node pacemaking. J Physiol 2004;559:835–48.
25. Papadatos GA, Wallerstein PM, Head CE, et al. Slowed conduction and ventricular tachycardia after targeted disruption of the cardiac sodium channel gene *SCN5A*. Proc Natl Acad Sci U S A 2002;99: 6210–5.
26. Asseman P, Berzin B, Desry D, et al. Persistent sinus nodal electrograms during abnormally prolonged postpacing atrial pauses in sick sinus syndrome in humans: sinoatrial block vs overdrive suppression. Circulation 1983;68:33–41.
27. Asseman P, Berzin B, Desry D, et al. Postextrasystolic sinoatrial exit block in human sick sinus syndrome: demonstration by direct recording of sinus node electrograms. Am Heart J 1991;122:1633–43.

Circ J 2005; **69:** 1543–1546

Effects of Late Administration of Immunoglobulin on Experimental Atherosclerosis in Apolipoprotein E-Deficient Mice

Taka-aki Okabe, MD; Chiharu Kishimoto, MD; Kana Shimada, MD; Toshinori Murayama, MD; Masayuki Yokode, MD; Toru Kita, MD

Background Although immunoglobulin treatment, beginning simultaneously with the initiation of atherosclerosis, suppresses experimental atherosclerosis in apolipoprotein E-deficient mice, it remains unclear whether the treatment at a subsequent stage of atherosclerosis would be effective.

Methods and Results Experimental atherosclerosis was induced in mice fed a high-fat diet containing 0.3% cholesterol. After confirming the presence of atherosclerotic lesions at 11 weeks, the mice were treated with an intraperitoneal injection of either intact type of immunoglobulin or F(ab')2 fragments of immunoglobulin (both, $1\,g\cdot kg^{-1}\cdot day^{-1}$) on alternate days over 4 weeks. Fatty streak lesion was suppressed by intact immunoglobulin administration, but not by F(ab')2 fragments of immunoglobulin. Immunohistochemical analysis showed that macrophage and $CD4^+$ T-cell accumulation in the fatty streak lesion was suppressed in mice that received intact immunoglobulin but not in those that received F(ab')2 fragments.

Conclusions Immunoglobulin treatment, even at a later stage of atherosclerosis, suppresses the development of lesions associated with the reduced expression of immune-activated cells in fatty streak plaques, demonstrating the benefits of immunoglobulin therapy for prevention of atherosclerosis. (*Circ J* 2005; **69:** 1543–1546)

Key Words: Atherosclerosis; F(ab')2 fragments; Fc portion; Immunoglobulin

Atherosclerosis is associated with immune activation and systemic immune responses and signs of inflammation.[1–3] Clinical investigations point to inflammatory/immune activation of plaque as a cause of acute coronary syndromes,[4,5] and seroepidemiological studies have suggested links between atherosclerosis and microbial infections.[4,6,7]

Therapy with immunoglobulin has been investigated in a wide range of immue-mediated disorders,[8–10] but the mode of action of immunoglobulin is still unclear. We have reported that the Fc portion of immunoglobulin has anti-inflammatory and immunomodulating actions in experimental and clinical studies of myocardial diseases.[10–12]

Recently, we also found that immunoglobulin treatment, given simultaneously with the development of the disease, suppresses atherosclerosis in apolipoprotein E (apo E)-deficient mice via the action of the Fc portion.[13] However, it remains unclear whether this treatment at a subsequent stage of atherosclerosis would be effective, so the current study was designed to evaluate this issue.

(Received May 31, 2005; revised manuscript received August 11, 2005; accepted August 29, 2005)

Department of Cardiovascular Medicine, Graduate School of Medicine, Kyoto University, Kyoto, Japan

Mailing address: Chiharu Kishimoto, MD, PhD, Department of Cardiovascular of Medicine, Graduate School of Medicine, Kyoto University, 54 Kawara-cho, Shogoin, Sakyo-ku, Kyoto 606-8507, Japan. E-mail: kkishi@kuhp.kyoto-u.ac.jp

Methods

Experimental Atherosclerosis

The apo E-deficient 129ola×C57BL/6 hybrid mice were the generous gift of Dr Edward M. Rubin (University of California, Berkeley, CA, USA). They were mated with C57BL/6 mice to produce F1 hybrids. The F1 apo $E^{+/-}$ mice were then backcrossed to C57BL/6 mice for 10 generations. Mice homogeneous for the apo E-null allele on a C57BL/6 background were subsequently generated. The mice were kept in a temperature-controlled facility on a 14.10-h light-dark cycle with free access to food and water. After being weaned at 4 weeks of age, mice were fed a normal chow diet until 6 weeks of age, when the animals were switched to a high-fat diet (HFD) containing 20% fat and 0.3% cholesterol as previously described.[13,14]

We performed animal experiments in accordance with the Declaration of Helsinki, and these were approved by our institutional ethics committee for animal experiments.

Immunoglobulin Treatment

After confirming by pathological examination the presence of atherosclerotic lesions in the apo-E deficient mice fed HFD over 5 weeks, intact human immunoglobulin (Venoglobulin-IH, Mitsubishi Pharma; a polyethylene glycol-treated human immunoglobulin) or F(ab')2 fragments of human immunoglobulin (Gamma-Venin, Aventis; a polyethylene glycol-treated human immunoglobulin) were intraperitoneally administered on alternate days at a dose of $1\,g\cdot kg^{-1}\cdot day^{-1}$ for another 4 week period (intact immunoglobulin, n=6; F(ab')2 fragments, n=6; controls, n=6). Littermate controls were injected with $1\,g\cdot kg^{-1}\cdot day^{-1}$ of human serum albumin (HSA) intraperitoneally. As

Table 1 Physiological Parameters

	n	BW (g)	TC (mg/dl)	TG (mg/dl)
HSA	6	26.4±0.7	811.2±126.7	55.3±7.8
Immunoglobulin	6	27.7±1.2	794.5±76.5	48.7±10.6
F(ab')2 fragments	6	28.0±0.9	804.7±115.0	51.7±12.8

Data are mean±SD.
HAS, human serum albumin; BW, body weight; TC, total cholesterol; TG, triglyceride.

shown in previous studies, immunoglobulin antigenecity between different species does not appear to be a problem[10,11,13] and furthermore both agents have the same chemical structure as the Fab portion of immunoglobulin.

Tissue Processing

Mice were killed by bleeding after puncturing the right ventricle. The blood was collected and allowed to clot. After the serum was separated, lipid profiles were analyzed. The vasculature was perfused with sterile phosphate-buffered saline. The root of the aorta was dissected under a macroscope and frozen in OCT embedding medium for serial cryosectioning covering 1.0 mm of the root. The first section was harvested when the first cusp became visible in the lumen of the aorta. Four sections of 10 μm thickness were harvested per slide, and thus 20 slides per mouse were prepared. All sections were immersed for 2 min in 60% isopropanol, stained for 15 min in a saturated oil red-O solution at 37°C, counterstained with hematoxylin, and then mounted under coverslips with glycerol gelatin.[13,14]

Quantitative Assessment of the Atherosclerotic Lesions

The oil red-O-stained sections were analyzed at a magnification of ×10, as previously described.[13,14] The image was captured directly from the RGB camera attached to a light microscope and displayed on a microcomputer to quantify the cross-sectional surface area of the lesion and the cross-sectional surface area of the vessel. The fractional area of the lesion was calculated by dividing the whole vessel area, including the lumen, intima, media and adventitia, as previously described. For each animal, 20 sections (ie, every 4th section) were examined, and the mean fractional area was calculated.[13,15]

Immunohistochemistry

Aortic root cryosections from mice treated with immunoglobulin, F(ab')2 fragments, or HSA were processed for immunohistochemistry as described previously.[11,12] In brief, anti-macrophage (anti-Mo, M3/84, 1:400, PharMingen, San Diego, CA, USA), anti-CD4 (GK1.5, 1:50, PharMingen), anti-CD8 (53–6.7, 1:50, PharMingen), and anti-I-A^b (25-9-17, 1:25, PharMingen) antibodies were applied to acetone-fixed cryosections. After being washed, the sections were then exposed to a second antibody (horseradish peroxidase-conjugated antibodies), and the antibody binding was visualized with diaminobenzidine. Sections were counterstained with 1% methyl green. The percentage of positively stained cells per cells infiltrating the lesions was calculated for each antibody, as previously described[13,14] (ie, lesions of the aortic root were analyzed). Data were obtained by dividing the number of positively stained cells by all methyl green-stained cells inside the internal elastic lamina. Three to 5 random microscopic fields were analyzed at ×200.

Fig 1. Effects of immunoglobulin and F(ab')2 fragments on atherosclerotic lesions. The lesions in the immunoglobulin-treated mice were smaller and covered a smaller fraction of the inner circumference of the aortic root than those in the control mice (arrows). However, the lesions in the F(ab')2 fragment-treated mice (arrows) were almost the same as those of the control mice (×40). HSA, human serum albumin.

Serum Lipid Measurement

Serum was separated by centrifugation and stored at −80°C. Serum total cholesterol and triglyceride levels were measured with assay kits (Wako) according to the manufacturer's instructions.

Statistical Analysis

Values were expressed as means±SD. Statistical analysis of the data was determined by one-way ANOVA, followed by the Fisher protected least-significant-difference test. A value of $p<0.05$ was considered statistically significant.

Results

Effects of Immunoglobulin

Physiological Parameters As shown in Table 1, treatment with the immunoglobulin preparations did not signifi-

Table 2 Quantitative Assessment of Atherosclerotic Lesions

	n	Lesion area, μm^2 (%)
HSA	6	115.0±57.9×10³ (14.7±7.4)
Immunoglobulin	6	48.5±18.0×10³ (6.2±2.3)*
F(ab')2 fragments	6	70.4±39.9×10³ (9.0±5.1)

*$p<0.05$ vs HSA. Data are mean±SD.
Atherosclerotic lesions were suppressed in mice that received immunoglobulin, but not in mice that received F(ab')2 fragments.

Table 3 Effects of Immunoglobulin and F(ab')2 Fragments on Inflammatory Cells in Lesions

	HSA	Immunoglobulin	F(ab')2 fragments
Mø (%)	14.3±6.1	2.8±2.1*	5.7±5.0
CD4+ (%)	18.1±7.7	5.9±3.2*	10.4±3.9
CD8+ (%)	7.2±4.0	3.9±3.0	5.5±2.1
I-Ab+ (%)	3.8±1.9	3.3±1.7	4.0±2.0

*$p<0.01$ vs HSA. Data are mean±SD.
Mø, macrophage.
Data were obtained by dividing the number of positively stained cells by all methyl green-stained cells inside the internal elastic lamina. Three to 5 random microscopic fields were analyzed at ×200. Treatment with immunoglobulin, but not with F(ab')2 fragments, reduced the expression of macrophage and CD4+ cells in the lesions.

Fig 2. Effects of immunoglobulin and F(ab')2 fragments on CD4+ cell accumulation in the lesions. Frequency of CD4+ cells (arrows) in immunoglobulin-treated mice was markedly decreased compared with F(ab')2 fragment-treated and control mice (×200). HSA, human serum albumin.

cantly modify the serum lipid profiles, nor did it have an affect on body weight.

Fatty Streak Formation Controls developed extensive lesions in the root of the aorta. Fatty streak lesions were suppressed by intact immunoglobulin administration, but not by F(ab')2 fragments (Fig 1). In mice treated with intact immunoglobulin, the fractional area of the lesion was significantly reduced (Table 2).

Expression of Inflammatory Cells Macrophage and CD4+ cell accumulation in the fatty streak lesions was suppressed in the mice that received intact immunoglobulin but not in those receiving F(ab')2 fragments (Table 3, Fig 2).

Discussion

This study clearly demonstrated that immunoglobulin treatment, even when initiated at a later stage of an experimental model of atherosclerosis, suppresses the development of the lesions associated with reduced expression of immune-activated cells in fatty streak plaques.

Intravenous immunoglobulin has been used to treat primary and secondary antibody deficiency for more than 25 years[8,9] It is a safe preparation with no long-term side effects. The therapy was first demonstrated to be effective for an autoimmune disorder (idiopathic thrombocytopenic purpura)[8] and since then, it has been established as effective in the treatment of Guillain-Barré syndrome, chronic inflammatory demyelinating polyneuropathy, myasthenia gravis, dermatomyositis and Kawasaki's syndrome, and in the prevention of graft-vs-host disease in recipients of allogenic bone marrow transplants[8-17] Benefits have been reported for many other autoimmune and systemic inflammatory conditions, but controlled trials are often lacking.

The mode of action of immunoglobulin is complex, involving modulation of the expression and function of Fc receptors, interference with the activation of complement and the cytokine network, provision of anti-idiotype antibodies, and effects on the activation, differentiation, and effector functions of T cells and B cells[8,9]

At present, atherosclerosis is considered to be the result of generalized inflammation associated with immune activation[1-3] We have already reported that immunoglobulin administration, beginning simultaneously with development of the disease, suppressed the lesions in experimental atherosclerosis via the actions of the Fc portion[13] In the clinical setting, however, the disease is subclinical; that is, most patients with atherosclerosis have small or moderate lesions when they begin treatment. Accordingly, in the current study, our aim was to clarify the effects of immunoglobulin in apo E-deficient mice that already had atherosclerotic lesions. Our results showed that immunoglobulin treatment at a subsequent stage of atherosclerosis suppressed the further development of lesions associated with the reduced expression of macrophage and CD4+ cells in the fatty streak plaque.

Some of the beneficial effects of immunoglobulin therapy in autoimmune and immune-mediated disorders have been attributed to the Fc portion of the drug[9,11,13,16] Indeed, from our data, treatment with the intact type, but not with F(ab')2 fragments, significantly suppressed the severity of atherosclerotic lesions associated with reduced expression of macrophages or CD4+ cells. Recent studies suggest that one mode of action of immunoglobulin is via

Fcγ receptor IIB, an inhibitory receptor, and that a large dose of immunoglobulin increases the expression this receptor![16] Accordingly, it may be that plaque is stabilized by this inhibitory receptor.

To date, there are no immunomodulating agents available for the prevention of atherosclerosis in the clinical setting![17,18] even though immune abnormalities are postulated as part of the disease's pathogenesis. Although there are some difficulties in the practical application of this therapy, exploration of the efficacy of this agent in human atherosclerosis appears warranted.

In conclusion, immunoglobulin administration, even at a subsequent stage in the progression of the disease, has the potential to reduce the development of lesions associated with the reduced expression of immune-activated cells in fatty streak plaques.

References

1. Ross R. Atherosclerosis: An inflammatory disease. *N Engl J Med* 1999; **340:** 115–126.
2. Hansson GK. Immune mechanisms in atherosclerosis. *Arterioscler Thromb Vasc Biol* 2001; **21:** 1876–1890.
3. Libby P, Hansson GK. Involvement of the immune system in human atherogenesis: Current knowledge and unanswered questions. *Lab Invest* 1991; **64:** 5–15.
4. Kawashiri MA, Higashikata T, Takata M, Katsuda S, Miwa K, Nohara A, et al. Type III hyperlipoproteinemia exaggerated by Sheehan's syndrome with advanced systemic atherosclerosis. *Circ J* 2005; **69:** 746–751.
5. Nasuno A, Matsubara T, Hori T, Higuchi K, Tsuchida K, Mezaki T, et al. Acute pulmonary thromboembolism induced by prophylactic heparin use and a heparin-coated catheter: A case of heparin-induced thrombocytopenia and thrombosis syndrome. *Circ J* 2003; **67:** 96–98.
6. Espinola-Klein C, Rupprecht HJ, Blankenberg S, Bickel C, Kopp H, Rippin G, et al. Impact of infectious burden on extent and long-term prognosis of atherosclerosis. *Circulation* 2002; **105:** 15–21.
7. Memon RA, Staprans I, Noor M, Holleran WM, Uchida Y, Moser AH, et al. Infection and inflammation induce LDL oxidation in vivo. *Arterioscler Thromb Vasc Biol* 2000; **20:** 1536–1542.
8. Godeau B, Chevret S, Varet B, Lefrere F, Zini JM, Bassompierre F, et al. Intravenous immunoglobulin or high-dose methylprednisolone, with or without oral prednisone, for adults with untreated severe autoimmune thrombocytopenic purpura: A randomized, multicentre trial. *Lancet* 2002; **359:** 23–29.
9. Kazatchkine MD, Kaveri SV. Immunodulation of autoimmune and inflammatory diseases with intravenous immune globulin. *N Engl J Med* 2001; **345:** 747–755.
10. Shioji K, Kishimoto C, Sasayama S. Fc receptor-mediated inhibitory effect of immunoglobulin therapy on autoimmune giant cell myocarditis: Concomitant suppression of the expression of dendritic cells. *Circ Res* 2001; **89:** 540–546.
11. Shioji K, Yuan Z, Kita T, Kishimoto C. Immunoglobulin treatment suppressed adoptively transferred autoimmune myocarditis in severe combined immunodeficient mice. *Am J Physiol* 2004; **287:** H2619–H2625.
12. Shioji K, Matsuura Y, Iwase T, Kitaguchi S, Nakamura H, Yodoi J, et al. Successful immunoglobulin treatment for fulminant myocarditis and serial analysis of serum thioredoxin: A case report. *Circ J* 2002; **66:** 977–980.
13. Yuan Z, Kishimoto C, Sano H, Shioji K, Xu Y, Yokode M. Immunoglobulin treatment suppresses atherosclerosis in apolipoprotein E-deficient mice via the Fc portion. *Am J Physiol* 2003; **285:** H899–H906.
14. Murayama T, Yokode M, Kataoka H, Imabayashi T, Yoshida H, Sano H, et al. Intraperitoneal administration of anti-c-*fms* monoclonal antibody prevents initial events of atherogenesis but dose not reduce the size of advanced lesions in apolipoprotein E-deficient mice. *Circulation* 1999; **99:** 1740–1746.
15. Nicoletti A, Kaveri S, Caligiuri G, Bariéty J, Hansson GK. Immunoglobulin treatment reduces atherosclerosis in apo E knockout mice. *J Clin Invest* 1998; **102:** 910–918.
16. Samuelsson A, Towers TL, Ravetch JV. Anti-inflammatory activity of IVIG mediated through the inhibitory Fc receptor. *Science* 2001; **291:** 484–486.
17. Kawashiri MA, Higashikata T, Noharara A, Kobayashi J, Inazu A, Koizumi J, et al. Efficacy of colestimide coadministered with atorvastatin in Japanese patients with heterozygous familial hypercholesterolemia (FH). *Circ J* 2005; **69:** 515–520.
18. Fan P, Zhang B, Kuroki S, Saku K. Pitavastatin, a potent hydroxymethylglutaryl coenzyme a reductase inhibitor, increases cholesterol 7 alpha-hydroxylase gene expression in HepG2 cells. *Circ J* 2004; **68:** 1061–1066.

Available online at www.sciencedirect.com
SCIENCE DIRECT
Neuroscience Letters 391 (2005) 1–6
Neuroscience Letters
www.elsevier.com/locate/neulet

Mechanism of impairment of long-term potentiation by amyloid β is independent of NMDA receptors or voltage-dependent calcium channels in hippocampal CA1 pyramidal neurons

Izumi Nomura[a], Nobuo Kato[b], Toru Kita[c], Hajime Takechi[a,*]

[a] *Department of Geriatric Medicine, Kyoto University Graduate School of Medicine, 54 Shogoin Kawahara-cho, Sakyo-ku, Kyoto 606-8507, Japan*
[b] *Department of Integrative Brain Science, Kyoto University Graduate School of Medicine, Kyoto 606-8507, Japan*
[c] *Department of Cardiovascular Medicine, Kyoto University Graduate School of Medicine, Kyoto 606-8507, Japan*

Received 6 June 2005; received in revised form 1 August 2005; accepted 12 August 2005

Abstract

β-Amyloid peptide (Aβ) is known to be involved in Alzheimer's disease (AD). Although the fibril form of Aβ is known to have neurotoxicity, it has been shown that not only the fibril form but also the oligomer form of Aβ may be related to the neuropathophysiology of AD, specifically to memory loss. Some studies have demonstrated that low concentrations of the Aβ oligomer impair long-term potentiation (LTP), a cellular model for learning and memory, after short exposure times in vivo and in vitro, although little is known about the mechanism involved in Aβ-mediated inhibition of LTP. In this study, we used the patch clamp whole-cell technique in rat hippocampal CA1 pyramidal neurons to study more precisely how the Aβ oligomer affects synaptic plasticity. The brief perfusion of slices with a low concentration (1 μM) of $A\beta_{1-42}$ significantly impaired LTP induction of the excitatory input. The same concentration of Aβ did not affect basal transmission or paired-pulse facilitation. We also demonstrated that neither NMDAR-EPSCs nor the voltage-depended calcium channel (VDCC) currents were affected by the same concentration of $A\beta_{1-42}$ as used in the LTP experiments. These data suggest that Aβ mediated impairment of LTP induction is independent of NMDARs or VDCCs.

Keywords: Alzheimer's disease; Amyloid β; Long-term potentiation (LTP); NMDA receptor; Calcium channel

Alzheimer's disease (AD) is a neurodegenerative disorder characterized by cognitive dysfunction. β-Amyloid peptide (Aβ) is known to be involved in the neuropathogenesis of AD. Aβ is a small protein which consists of 39–43 amino acid residues. Aβ can exist in different forms, including monomers, oligomers, protofibrils, and fibrils. It is known that Aβ monomers aggregate into self-assembled fibrillar structures. Because the fibrils are known to induce cell death in culture, it has been argued that deposits of Aβ are critically responsible for the neurodegeneration that occurs in AD [8]. However, there is evidence against this argument. For example, the pathological analysis of postmortem AD brains revealed that fibrillar Aβ density is not strongly correlated with the severity of AD [1,19,20]. Mucke et al. [16] also showed that amyloid plaque formation appears after the onset of cognitive defects in AD transgenic mice. Recent reports suggest that the toxicity of Aβ lies not only in the fibril form but also in soluble oligomeric species [5,11]. Consistently, some reports demonstrated that low concentrations of the Aβ oligomer impaired long-term potentiation (LTP), a form of synaptic plasticity, without affecting basal synaptic transmission in normal mice or rats in vivo [6,10] and in vitro [2,17,22–24].

Although the mechanism by which Aβ induces cell death has been extensively studied, it is not clearly known how Aβ oligomers inhibit LTP. From a pharmacokinetic point of view, the facts that the effect on synaptic plasticity is induced within a relatively short time and with low concentrations of Aβ suggest that there is a mechanism distinct from that causing cell death. Gong et al. [7] demonstrated that the oligomer form of Aβ was bound to clustered rafts or synaptic terminals of cultured rat hippocampal neurons when low concentrations of soluble Aβ were applied for 5 min. Kourie [12] reviewed the studies that Aβ alters cell regulation by modifying several ion transport systems. These reports suggest that Aβ might function at the synapse as a specific ligand. Among synaptic membrane proteins, the *N*-methyl-D-aspartate receptor (NMDAR) and voltage-dependent calcium channels (VDCCs) seem to play central roles in the

* Corresponding author. Tel.: +81 75 751 3460; fax: +81 75 751 3264.
E-mail address: takechi@kuhp.kyoto-u.ac.jp (H. Takechi).

0304-3940/$ – see front matter © 2005 Elsevier Ireland Ltd. All rights reserved.
doi:10.1016/j.neulet.2005.08.024

induction of LTP [4]. It might be possible that this receptor and these channels are the targets of Aβ-mediated impairment of LTP induction. In terms of NMDAR-mediated excitatory postsynaptic currents (NMDAR-EPSCs), the results were controversial. Wu et al. [25] reported that NMDAR-EPSCs were enhanced, but others reported the opposite results [3,17] by the application of soluble Aβ. As for VDCC, it was reported that VDCC currents were elevated by the application of low concentrations of Aβ oligomers [14,18]. However, to date, no report has examined VDCC currents using the same conditions as used in the LTP experiments. In this study, therefore, we used the patch clamp whole-cell technique in rat hippocampal CA1 pyramidal neurons to investigate the effects of Aβ on both LTP and relevant receptors and ion channels under the same experimental conditions.

All experiments were performed in accordance with the guiding principles of the Physiological Society of Japan and with the approval of the Animal Care Committee of Kyoto University Graduate School of Medicine. Slices (400 μm thick) of the hippocampus were prepared from Wister rats (19–21 days old) with a microslicer DTK-1000 (Dosaka, Kyoto, Japan). Slices were kept at room temperature for at least 60 min before experiments in normal medium composed (in mM) of NaCl 124, KCl 3.0, $CaCl_2$ 2.5, $MgCl_2$ 1.25, NaH_2PO_4 1.3, $NaHCO_3$ 26, and glucose 11, bubbled with a mixture of 95% O_2 and 5% CO_2. The chamber was continuously perfused with the medium at room temperature (~25 °C), bubbled with a mixture of 95% O_2 and 5% CO_2. In all experiments, in order to block the actions of GABA receptors, bicuculline (10 μM) and CGP55854 (1 μM), were added.

Whole-cell recordings were made from the soma of visually identified pyramidal neurons located in CA1 of the hippocampus. Patch pipettes (5–7 MΩ) were filled with an internal solution containing (in mM) $CsMeSO_3$ 120, CsCl 5, $MgCl_2$ 2, HEPES 10, EGTA 0.2, Na_2ATP 2, GTP 0.4, NaCl 5, and QX-314 5, pH adjusted to 7.3 with CsOH and 290 mOsm. Series resistance was always 15–35 MΩ and was monitored throughout each experiment. Cells were excluded from data analysis if more than a 20% change in series resistance occurred during the course of the experiment. Holding potentials were −70 mV. The EPSC-9 patch-clamp amplifier and program package PULSE-PULSEFIT (HEKA Electronics, Lambrecht, Germany) were used for data acquisition.

Excitatory postsynaptic currents (EPSCs) were evoked using stimulating glass capillary microelectrodes filled with the normal medium placed in the stratum radiatum. Synaptic responses were generated by stimulating Schaffer collateral/commissural projections at 0.05 Hz. Stable baseline recordings were made for more than 5 min prior to LTP induction. LTP induction was attempted within 20 min after whole-cell break-in. LTP was

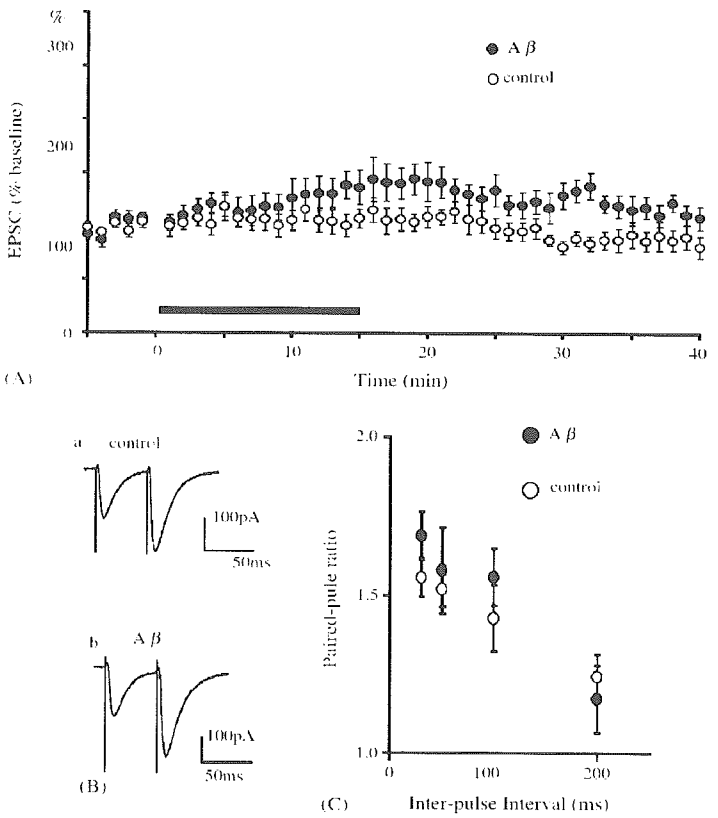

Fig. 1. $A\beta_{1-42}$ did not affect basal synaptic transmission or paired-pulse facilitation. (A) Pooled data (mean ± S.E.M.) showing basal synaptic transmission for control cells (open circles: $n = 13$) and Aβ treated cells (closed circles: $n = 11$). (B) Representative EPSC traces by paired stimuli in control cells (a) and Aβ treated slices (b) at a 50 ms interstimulus interval. (C) The ratios of the amplitude of pulse2 pulse1 with various pulse intervals (30, 50, 100, and 200 ms) for control slices (open circles) and Aβ-treated slices (closed circles).

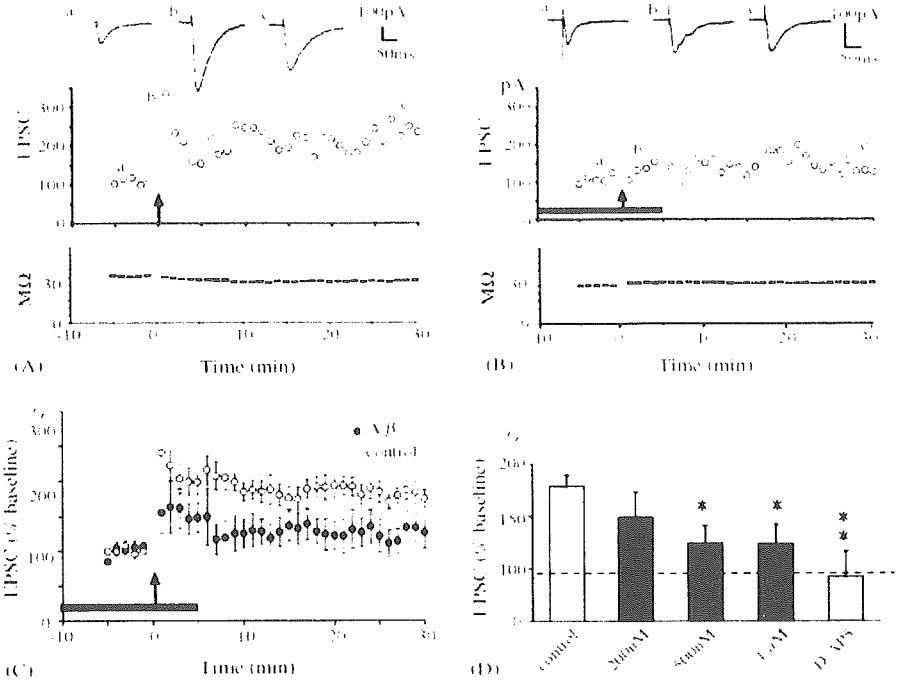

Fig. 2. $A\beta_{1-42}$ dose-dependently impaired NMDAR-dependent LTP induction under the whole-cell recordings from CA1 pyramidal cells. (A) A representative experiment of control LTP induction. Series resistance is shown at the bottom. Each point represents the mean of three EPSCs. Insets show typical traces of recordings at the times indicated. (B) A representative LTP experiment in the presence of perfusion of Aβ (1 μM) for 15 min. Aβ application is indicated by a black bar. (C) Pooled data (mean ± S.E.M.) from control cells (open circles; $n = 15$) and Aβ-treated cells (closed circles; $n = 11$). (D) Average amplitude of EPSCs measured 25–30 min after LTP induction with medium (control), Aβ 200 nM, Aβ 500 nM, Aβ 1 μM and the NMDA-R antagonist, D-AP5, respectively. Values are the mean ± S.E.M. $^{*}p < 0.05$, $^{**}p < 0.01$.

induced by 10 theta-bursts with a short depolarization to 0 mV for 50 ms. Depolarization was given for each burst. Each burst contained four pulses at 100 Hz, and the bursts themselves were separated by 200 ms. Paired-pulse experiments were conducted under the same conditions using four paired-pulse protocols having interpulse intervals of 30, 50, 100, and 200 ms. To measure VDCC currents, the medium contained (mM) NaCl 100, KCl 3.0, $BaCl_2$ 2.5, $MgCl_2$ 1.25, $NaHCO_3$ 26, $CsCl_2$ 5, TEA 20, 4-amynopyridine 0.5, tetrodotxin (TTX) 0.001 and glucose 11. $BaCl_2$ was used as the carrier to record the Ca^{2+} current. Barium currents (I_{Ba}) were evoked by a 150 ms depolarizing step to 0 mV (from a holding potential of −60 mV) at 0.1 Hz.

$A\beta_{1-42}$ and $A\beta_{25-35}$ were purchased from Peptide Institute, Inc. (Osaka, Japan). They were dissolved in DMSO (1 mM) and aliquoted before freezing at −20 °C. Aβ was diluted to the desired final concentrations in medium before application in each experiment. Depending on the purpose of each experiment, we bath-applied one of the following drugs: D-AP5 (50 μM), nimodipine (3 μM) or $NiCl_2$ (500 μM). Ni^{2+} blocks all subtypes of VDCCs at this concentration. All the drugs were purchased from Nacalai Ltd. (Kyoto, Japan) unless otherwise noted.

Recorded data were analyzed with StatView 4.0 (North Caroline, USA). Data are expressed as means ± S.E.M. Student's *t*-test was used for statistical analysis with the significance level set at $p < 0.05$.

We first checked the effect of $A\beta_{1-42}$ (1 μM) on normal synaptic transmission. Although Aβ slightly enhanced basal

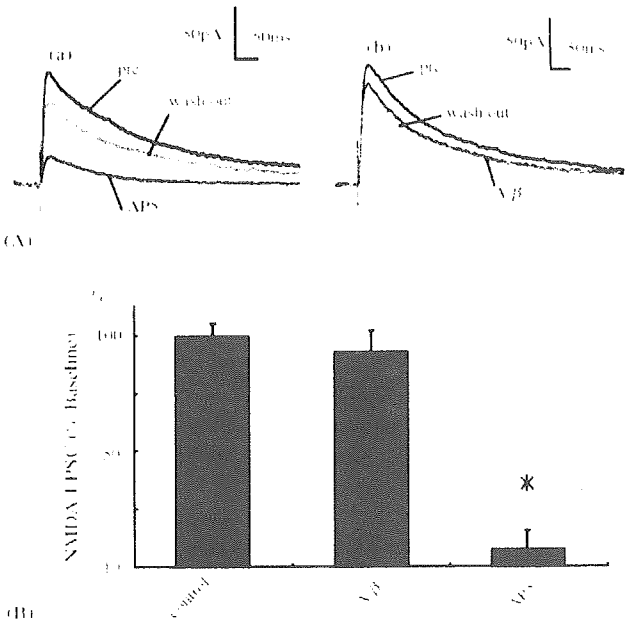

Fig. 3. $A\beta_{1-42}$ induced no significant changes in NMDA receptor-mediated EPSCs. (A) Representative traces of NMDAR current evoked by synaptic stimulus when AP5 (a) or Aβ (b) was applied for 10 min and washed out. The traces were obtained by averaging 15 waves from 5 min recordings in each period indicated. (B) Average of the peak amplitude of NMDAR-EPSCs 10–15 min after the application of control medium, Aβ or AP5. The bars are scaled to set the control value as 100%. $^{*}p < 0.01$.

synaptic transmission, there was no significant difference in the EPSC amplitude between control cells (98 ± 13%; n = 13) and those applied with Aβ (114 ± 8%; n = 11; $p > 0.10$), measured during the last 5 min of the recording period 25–30 min after normal or Aβ medium perfusion (Fig. 1A). To examine the effect of Aβ (1 μM) on short-term plasticity, we recorded paired-pulse facilitation (PPF) (Fig. 1B). With none of the interstimulus-intervals tested, did paired-pulse ratios differ between control and Aβ treated cells (Fig. 1C).

After medium containing $A\beta_{1-42}$ or the NMDA receptor antagonist, D-AP5, was perfused for 10 min, high frequency stimulation (HFS) was given and drugs were washed out 5 min after HFS (Fig. 2). HFS evoked LTP in control slices but failed to evoke LTP in slices perfused with Aβ. Representative experiments are shown in Fig. 2A (control) and 2B (Aβ 1 μM). The mean data from all the experiments of control cells and $A\beta_{1-42}$ (1 μM) treated cells are summarized in Fig. 2C. The amount of LTP was determined by calculating the mean of the EPSC amplitude from 25 to 30 min after HFS (Fig. 2D). The peak EPSC amplitude was potentiated to 179 ± 11% (n = 15) of baseline in control cells, while it was 93 ± 21% (n = 7) in D-AP5 (50 μM) treated cells. Perfusion with D-AP5 significantly inhibited the induction of LTP. Thus, this LTP induction was dependent on the activation of NMDA receptors. Bath application of 500 nM and 1 μM of Aβ significantly impaired LTP induction (124 ± 16%; n = 7; $p < 0.01$ in 500 nM, and 125 ± 14%; n = 11; $p < 0.01$ in 1 μM), while 200 nM of Aβ failed to impair LTP induction (149 ± 22; n = 7; $p > 0.1$). Thus, Aβ dose-dependently impaired NMDAR-dependent LTP induction.

To measure NMDAR-EPSC's, cells were held at +40 mV in the presence of 10 μM CNQX. Presynaptic stimulation was applied and the amount of NMDAR-EPSC's was determined by calculating the mean of the EPSC amplitude from 10 to 15 min after medium or drug perfusion. Representative traces are shown in Fig. 3A. Addition of the NMDA receptor antagonist D-AP5 (50 μM) almost abolished NMDAR-EPSC's (26 ± 6%; n = 4; $p < 0.001$ compared to the control group; 100 ± 4%; n = 6). $A\beta_{1-42}$ (1 μM) did not affect NMDAR-EPSC's (95 ± 7%; n = 6; $p > 0.05$) (Fig. 3B). There was also no significant difference in the charge transfer thorough NMDAR-EPSC's between the control and $A\beta_{1-42}$ groups (control; 100 ± 4%, $A\beta_{1-42}$; 94 ± 7%; $p > 0.50$). After washing for 15 min, the reduction of NMDAR-EPSC's by AP5 was recovered (87 ± 14%; n = 4; $p > 0.1$).

Then, we examined VDCC mediated barium currents (I_{Ba}). Time courses of I_{Ba} change during the 10 min after the application of various drugs are presented in Fig. 4A. The amplitude of inward I_{Ba} was measured at the peak. Representative traces are shown in Fig. 4B. The L-type VDCC blocker, nimodipine (3 μM), decreased I_{Ba} significantly (83 ± 5%; n = 5; $p < 0.05$) compared with control group (100 ± 3%; n = 14) and

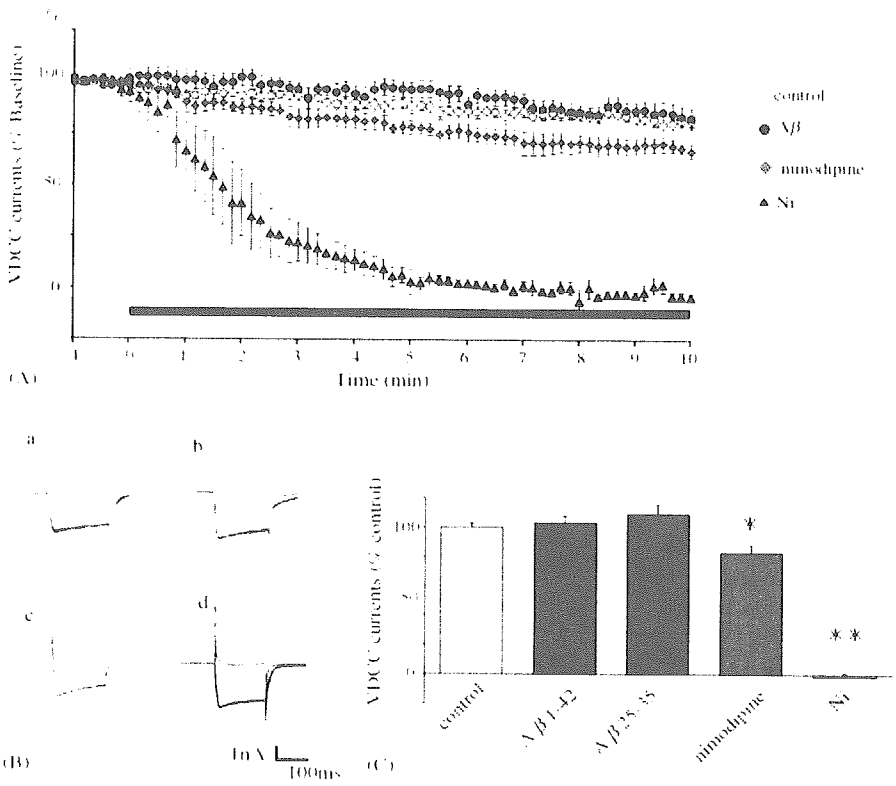

Fig. 4. Aβ used under the same conditions as in the LTP experiment failed to affect VDCC currents. (A) Time courses of the experiments are shown. The time of drug application is indicated by the horizontal bar. Pooled data are calculated as the percentage of means compared to the baseline value. (B) Current traces of I_{Ba} before (black traces) and 10 min after (gray traces) the applications of medium (a), $A\beta_{1-42}$ (b), L-type VDCC blocker, nimodipine (c), and a high concentration of Ni^{2+} (500 μM) are shown. (C) The averaged peak amplitudes of VDCC currents 8–10 min after drug application are shown. The data are expressed as percentages of the control. Values are the mean ± S.E.M. $^{*}p < 0.05$, $^{**}p < 0.01$.

Ni^{2+} (500 μM) abolished I_{Ba} ($-1.4 \pm 2.5\%$; $n = 4$; $p < 0.0001$). $A\beta_{1-42}$ (1 μM), however, did not affect I_{Ba} ($A\beta_{1-42}$; $103 \pm 4\%$; $n = 10$; $p > 0.50$). We also examined another species of Aβ, $A\beta_{25-35}$. $A\beta_{25-35}$ (1 μM) did not affect I_{Ba} either ($A\beta_{25-35}$; $109 \pm 7\%$; $n = 6$; $p > 0.10$). The mean VDCC currents (percent of control group) measured at 8–10 min after drug application are shown in Fig. 4C. We also examined VDCC currents in the normal medium which contained Ca^{2+} instead of Ba^{2+}. $A\beta_{1-42}$ did not affect calcium currents (control; $100 \pm 4\%$; $n = 4$, $A\beta_{1-42}$; $100 \pm 8\%$; $n = 3$; $p > 0.50$).

In this study, we demonstrated that low concentrations of soluble $A\beta_{1-42}$ impair LTP induction without affecting basal synaptic transmission using the patch clamp whole-cell technique in rat hippocampal CA1 pyramidal neurons, and that under the same conditions, neither NMDAR-EPSCs nor VDCC currents are affected by Aβ.

NMDARs play a pivotal role in the LTP induction of CA1 pyramidal neurons, and hence the modulation of NMDAR function is a potential target for the inhibitory action of Aβ. The data that $A\beta_{1-42}$ inhibits NMDAR-dependent LTP, but not NMDAR-independent LTP [26] may indicate the involvement of NMDARs in the Aβ-mediated inhibition of LTP induction. Although the increase in NMDAR-mediated current by Aβ was shown in rat dentate granule cells [25], later reports claimed it decreased, not increased, in rat dentate granule cells or in rat CA1 pyramidal neurons [3,17]. Raymond et al. [17] also described the slight inhibition of NMDAR by $A\beta_{1-40}$, and showed that it did not affect LTP induction. In contrast, our data showed no apparent effect of $A\beta_{1-42}$ on NMDAR-EPSCs in CA1 pyramidal neurons. Our results suggest that NMDAR is not the primary target of inhibitory action of Aβ in terms of LTP induction. Aβ may rather affect a downstream pathway of NMDAR signaling, into which upstream molecules other than NMDARs may converge. In connection with this, it has recently been reported that the phosphorylation of CaMKII, a kinase that transduces LTP-inducing NMDAR activity, is inhibited by Aβ [26].

VDCC is also a potential target of Aβ-mediated impairment of LTP induction. It has been reported that calcium homeostasis is disturbed by Aβ, and that this is one of the most important reasons for the apoptotic action of Aβ [9,13–15,18,21]. There are, however, only a few reports that have examined the role of VDCC along the new hypothesis that low concentrations of Aβ oligomers inhibit synaptic plasticity. Li et al. [14] showed that a two-fold increase in I_{Ba} is observed after 5 min exposure to 1 μM $A\beta_{1-40}$ in cultured rat hippocampal neurons. Rovia et al. [18] showed that 200 nM $A\beta_{25-35}$ and $A\beta_{1-40}$ increase VDCC currents in rat CA1 pyramidal neurons. Although it is important to study the relationship between VDCC activation and the inhibitory effects on LTP, they were not simultaneously studied in these reports. Here, in this report, we demonstrated for the first time that there are no significant changes in VDCC current caused by Aβ under the same conditions as used in our LTP experiments, in which Aβ clearly inhibited LTP induction. Further investigations to clarify these mechanisms are important in order to find an efficient treatment for AD.

References

[1] P.V. Arriagada, J.H. Growdon, E.T. Hedley-Whyte, B.T. Hyman, Neurofibrillary tangles but not senile plaques parallel duration and severity of Alzheimer's disease, Neurology 42 (1992) 631–639.

[2] Q.S. Chen, B.L. Kagan, Y. Hirakura, C.W. Xie, Impairment of hippocampal long-term potentiation by Alzheimer amyloid β-peptides, J. Neurosci. Res. 60 (2000) 65–72.

[3] Q.S. Chen, W.Z. Wei, T. Shimahara, C.W. Xie, Alzheimer amyloid β-peptide inhibits the late phase of long-term potentiation through calcineurin-dependent mechanisms in the hippocampal dentate gyrus, Neurobiol. Learn. Mem. 77 (2002) 354–371.

[4] R. Chittajallu, S. Alford, G.L. Collingridge, Ca^{2+} and synaptic plasticity, Cell Calcium 24 (1998) 3773–3785.

[5] F.G. De Felice, M.N. Vieira, L.M. Saraiva, J.D. Figueroa-Villar, J. Garcia-Abreu, R. Liu, L. Chang, W.L. Klein, S.T. Ferreira, Targeting the neurotoxic species in Alzheimer's disease: inhibitors of Aβ oligomerization, FASEB J. (2004) 1366–1372.

[6] D.B. Freir, C. Holscher, C.E. Herron, Blockade of long-term potentiation by β-amyloid peptides in the CA1 region of the rat hippocampus in vivo, J. Neurophysiol. 85 (2001) 708–713.

[7] Y. Gong, L. Chang, K.L. Viola, P.N. Lacor, M.P. Lambert, C.E. Finch, G.A. Krafft, W.L. Klein, Alzheimer's disease-affected brain: presence of oligomeric Aβ ligands (ADDLs) suggests a molecular basis for reversible memory loss, Proc. Natl. Acad. Sci. U.S.A. 100 (2003) 10417–10422.

[8] J.A. Hardy, G.A. Higgins, Alzheimer's disease: the amyloid cascade hypothesis, Science 256 (1992) 184–185.

[9] L.M. He, L.Y. Chen, X.L. Lou, A.L. Qu, Z. Zhou, T. Xu, Evaluation of β-amyloid peptide 25–35 on calcium homeostasis in cultured rat dorsal root ganglion neurons, Brain Res. 939 (2002) 65–75.

[10] A. Itoh, T. Akaike, M. Sokabe, A. Nitta, R. Iida, A. Olariu, K. Yamada, T. Nabeshima, Impairments of long-term potentiation in hippocampal slices of β-amyloid-infused rats, Eur. J. Pharmacol. 382 (1999) 167–175.

[11] W.L. Klein, G.A. Krafft, C.E. Finch, Targeting small Aβ oligomers: the solution to an Alzheimer's disease conundrum? Trends Neurosci. 24 (2001) 219–224.

[12] J.I. Kourie, Mechanisms of amyloid β protein-induced modification in ion transport systems: implications for neurodegenerative diseases, Cell Mol. Neurobiol. 21 (2001) 173–213.

[13] F.M. LaFerla, Calcium dyshomeostasis and intracellular signalling in Alzheimer's disease, Nat. Rev. Neurosci. 3 (2002) 862–872.

[14] W.Y. Li, J.P. Butler, J.E. Hale, D.B. McClure, S.P. Little, D.L. Czilli, L.K. Simmons, Suppression of an amyloid β peptide-mediated calcium channel response by a secreted β-amyloid precursor protein, Neuroscience 95 (2000) 1–4.

[15] A. MacManus, M. Ramsden, M. Murray, Z. Henderson, H.A. Pearson, V.A. Campbell, Enhancement of $^{45}Ca^{2+}$ influx and voltage-dependent Ca^{2+} channel activity by beta-amyloid-(1–40) in rat cortical synaptosomes and cultured cortical neurons. Modulation by the proinflammatory cytokine interleukin-1β, J. Biol. Chem. 275 (2000) 4713–4718.

[16] L. Mucke, E. Masliah, G.Q. Yu, M. Mallory, E.M. Rockenstein, G. Tatsuno, K. Hu, D. Kholodenko, K. Johnson-Wood, L. McConlogue, High-level neuronal expression of Aβ 1–42 in wild-type human amyloid protein precursor transgenic mice: synaptotoxicity without plaque formation, J. Neurosci. 20 (2000) 4050–4058.

[17] C.R. Raymond, D.R. Ireland, W.C. Abraham, NMDA receptor regulation by amyloid-β does not account for its inhibition of LTP in rat hippocampus, Brain Res. 968 (2003) 263–272.

[18] C. Rovira, N. Arbez, J. Mariani, Aβ (25–35) and Aβ (1–40) act on different calcium channels in CA1 hippocampal neurons, Biochem. Biophys. Res. Commun. 296 (2002) 1317–1321.

[19] W. Samuel, R.D. Terry, R. DeTeresa, N. Butters, E. Masliah, Clinical correlates of cortical and nucleus basalis pathology in Alzheimer dementia, Arch. Neurol. 51 (1994) 772–778.

[20] R.D. Terry, E. Masliah, D.P. Salmon, N. Butters, R. DeTeresa, R. Hill, L.A. Hansen, R. Katzman, Physical basis of cognitive alterations in

Alzheimer's disease: synapse loss is the major correlate of cognitive impairment, Ann. Neurol. 30 (1991) 572–580.

[21] K. Ueda, S. Shinohara, T. Yagami, K. Asakura, K. Kawasaki, Amyloid β protein potentiates Ca^{2+} influx through L-type voltage-sensitive Ca^{2+} channels: a possible involvement of free radicals, J. Neurochem. 68 (1997) 265–271.

[22] D.M. Walsh, I. Klyubin, J.V. Fadeeva, W.K. Cullen, R. Anwyl, M.S. Wolfe, M.J. Rowan, D.J. Selkoe, Naturally secreted oligomers of amyloid β protein potently inhibit hippocampal long-term potentiation in vivo, Nature 416 (2002) 535–539.

[23] Q. Wang, M.J. Rowan, R. Anwyl, β-Amyloid-mediated inhibition of NMDA receptor-dependent long-term potentiation induction involves activation of microglia and stimulation of inducible nitric oxide synthase and superoxide, J. Neurosci. 24 (2004) 6049–6056.

[24] Q. Wang, D.M. Walsh, M.J. Rowan, D.J. Selkoe, R. Anwyl, Block of long-term potentiation by naturally secreted and synthetic amyloid β-peptide in hippocampal slices is mediated via activation of the kinases c-Jun N-terminal kinase, cyclin-dependent kinase 5, and p38 mitogen-activated protein kinase as well as metabotropic glutamate receptor type 5, J. Neurosci. 24 (2004) 3370–3378.

[25] J. Wu, R. Anwyl, M.J. Rowan, β-Amyloid selectively augments NMDA receptor-mediated synaptic transmission in rat hippocampus, NeuroReport 27 (1995) 2409–2413.

[26] D. Zhao, J.B. Watson, C.W. Xie, Amyloid β prevents activation of calcium calmodulin-dependent protein kinase II and AMPA receptor phosphorylation during hippocampal long-term potentiation, J. Neurophysiol. 92 (2004) 2853–2858.